A&A 595, A42 (2016)
DOI: 10.1051/0004-6361/201628183

Astronomy & Astrophysics

The XMM Cluster Outskirts Project (X-COP): Physical conditions of Abell 2142 up to the virial radius

C. Tchernin[1,2], D. Eckert[2,3], S. Ettori[4,5], E. Pointecouteau[6,11], S. Paltani[2], S. Molendi[3], G. Hurier[7,12], F. Gastaldello[3,8], E. T. Lau[9], D. Nagai[9], M. Roncarelli[4], and M. Rossetti[10,3]

[1] Center for Astronomy, Institute for Theoretical Astrophysics, Heidelberg University, Philosophenweg 12, 69120 Heidelberg, Germany
e-mail: Tchernin@uni-heidelberg.de
[2] Department of Astronomy, University of Geneva, ch. d'Ecogia 16, 1290 Versoix, Switzerland
[3] INAF–IASF-Milano, via E. Bassini 15, 20133 Milano, Italy
[4] INAF–Osservatorio Astronomico di Bologna, via Ranzani 1, 40127 Bologna, Italy
[5] INFN, Sezione di Bologna, viale Berti Pichat 6/2, 40127 Bologna, Italy
[6] CNRS, IRAP, 9 Av. colonel Roche, BP 44346, 31028 Toulouse Cedex 4, France
[7] Centro de Estudios de Fisica del Cosmos de Aragon, Plaza San Juan 1, Planta-2, 44001 Teruel, Spain
[8] Department of Physics and Astronomy, University of California at Irvine, 4129 Frederick Reines Hall, Irvine, CA 92697-4575, USA
[9] Department of Physics, Yale University, New Haven, CT 06520, USA
[10] Università degli studi di Milano, Dip. di Fisica, via Celoria 16, 20133 Milano, Italy
[11] Université de Toulouse, UPS-OMP, IRAP, 38000 Toulouse, France
[12] Institut d'Astrophysique Spatiale, CNRS, UMR8617, Université Paris-Sud 11, Batiment 121, Orsay, France

Received 25 January 2016 / Accepted 17 June 2016

ABSTRACT

Context. Galaxy clusters are continuously growing through the accretion of matter in their outskirts. This process induces inhomogeneities in the gas density distribution (clumping) that need to be taken into account to recover the physical properties of the intracluster medium (ICM) at large radii.
Aims. We studied the thermodynamic properties in the outskirts ($R > R_{500}$) of the massive galaxy cluster Abell 2142 by combining the Sunyaev Zel'dovich (SZ) effect with the X-ray signal.
Methods. We combined the SZ pressure profile measured by *Planck* with the *XMM-Newton* gas density profile to recover radial profiles of temperature, entropy, and hydrostatic mass out to $2 \times R_{500}$. We used a method that is insensitive to clumping to recover the gas density, and we compared the results with traditional X-ray measurement techniques.
Results. When taking clumping into account, our joint X-SZ entropy profile is consistent with the predictions from pure gravitational collapse, whereas a significant entropy flattening is found when the effect of clumping is neglected. The hydrostatic mass profile recovered using joint X-SZ data agrees with that obtained from spectroscopic X-ray measurements and with mass reconstructions obtained through weak lensing and galaxy kinematics.
Conclusions. We found that clumping can explain the entropy flattening observed by *Suzaku* in the outskirts of several clusters. When using a method that is insensitive to clumping for the reconstruction of the gas density, the thermodynamic properties of Abell 2142 are compatible with the assumption that the thermal gas pressure sustains gravity and that the entropy is injected at accretion shocks, with no need to evoke more exotic physics. Our results highlight the need for X-ray observations with sufficient spatial resolution, and large collecting area, to understand the processes at work in cluster outer regions.

Key words. X-rays: galaxies: clusters – radiation mechanisms: thermal – galaxies: clusters: intracluster medium – cosmology: observations – submillimeter: general

1. Introduction

Galaxy clusters are the largest gravitationally bound systems in the Universe. According to the concordance cosmological model, they are the latest structures to be formed. For this reason, they are expected to continue growing at the present epoch through the accretion of matter in their outskirts. Thus, information on the processes governing structure formation can be obtained through the study of galaxy cluster outskirts (see Reiprich et al. 2013, for a review). The distribution of matter in the outer regions of galaxy clusters is expected to become clumpy (Nagai & Lau 2011; Vazza et al. 2013) and asymmetric (Vazza et al. 2011), and the impact of nonthermal energy in the form of turbulence, bulk motions, cosmic rays, and magnetic fields is expected to be significant, even if still poorly constrained by theory and simulations.

Spectroscopic X-ray measurements of cluster outskirts became possible recently with the *Suzaku* experiment thanks to its low particle background (Mitsuda et al. 2007). With the help of *Suzaku*, many bright galaxy clusters have been observed out to the viral radius ($\sim R_{200}$; e.g., Reiprich et al. 2009; Hoshino et al. 2010; Akamatsu et al. 2011; Simionescu et al. 2011; Walker et al. 2012, 2013; Urban et al. 2014; Okabe et al. 2014). These works studied the radial profiles of the density, temperature, and entropy out to R_{200}. In several cases, the authors observed a flattening of the entropy profile beyond R_{500}

compared to the expectation of the self-similar accretion model (Voit et al. 2005). Several studies also observed a decrease in the hydrostatic mass profile in the same radial range, which might suggest that the medium is out of hydrostatic equilibrium. This could be caused by a significant nonthermal pressure in the form of turbulence, bulk motions, or cosmic rays (e.g., Vazza et al. 2009; Lau et al. 2009; Battaglia et al. 2013), nonequilibration between electrons and ions (Hoshino et al. 2010; Avestruz et al. 2015), or weakening of the accretion shocks (Lapi et al. 2010; Fusco-Femiano & Lapi 2014).

Alternatively, Simionescu et al. (2011) proposed that the measured gas density is overestimated because of gas clumping, which would lead to an underestimated entropy (see also Eckert et al. 2013b; Walker et al. 2013; Urban et al. 2014; Morandi et al. 2013; Morandi & Cui 2014). Recently, several numerical studies have focused on quantifying the effect of gas inhomogeneities on X-ray observations (see, e.g., Nagai & Lau 2011; Zhuravleva et al. 2013; Eckert et al. 2015; Vazza et al. 2013; Roncarelli et al. 2013). For instance, using hydrodynamical simulations Zhuravleva et al. (2013) showed that the density distribution inside a shell at a given distance from the cluster center can be described by a lognormal distribution plus a high-density tail (see also Rasia et al. 2014; Khedekar et al. 2013). While the lognormal distribution contains information about the bulk of the intracluster medium (ICM), the high-density tail is due to the presence of infalling gas clumps. The authors showed that the median of the distribution coincides with the mode of the lognormal distribution, whereas the mean is biased high by the presence of clumps. This result has been confirmed observationally by Eckert et al. (2015), where the authors reproduced this result using ROSAT and *XMM-Newton* data. These authors computed the surface-brightness distribution in an annulus at $\sim 1.2 \times R_{500}$ from the cluster center and showed that the median of the distribution corresponds to the mode of the lognormal distribution, while the mean is shifted toward higher surface-brightness values. They concluded that the azimuthal median method allows us to recover the true gas density profile even in the presence of inhomogeneities.

In addition, the recent years have seen great progress in the study of the ICM through the Sunyaev-Zel'dovich (SZ) effect (Sunyaev & Zeldovich 1972). The SZ effect arises when photons of the cosmic microwave background photons (CMB) interact with the electrons of the ICM through inverse Compton scattering. The observed distortion of the CMB spectrum is proportional to the thermal electron pressure integrated along the line of sight (the Compton y parameter). Therefore, the SZ signal decreases less sharply with radius than the X-ray emissivity. Furthermore, it is less sensitive to density inhomogeneities. Indeed, it has been shown that at R_{200}, variations in the X-ray signal are ~3 times larger than in the SZ flux (see for instance Fig. 6 of Roncarelli et al. 2013) since the fluctuations are nearly isobaric (Khedekar et al. 2013). This makes the SZ signal highly complementary to X-ray observations. Recent SZ experiments (e.g., *Planck*, Bolocam, SPT) enabled us to extend the measurements of the SZ signal well beyond R_{500} (Planck Collaboration Int. V 2013; Sayers et al. 2013). These breakthroughs opened the possibility of combining the SZ signal with X-ray observations to study the thermodynamical properties of the gas, thereby bypassing the use of X-ray spectroscopic data (Ameglio et al. 2007; Nord et al. 2009; Basu et al. 2010; Eckert et al. 2013a). Joint X-ray and SZ imaging studies can also lead to a reconstruction of the cluster mass profile through the hydrostatic equilibrium assumption (Ameglio et al. 2009; Eckert et al. 2013b).

In this paper, we combine SZ and X-ray observations (X-SZ) from the *Planck* and *XMM-Newton* satellites to study the outskirts of Abell 2142. This cluster belongs to the sample selected in the framework of the XMM Cluster Outskirts Project (X-COP), a very large program on *XMM-Newton* which aims at studying the outskirts of an SZ-selected sample of 13 massive, nearby clusters. Abell 2142 is a massive cluster ($M_{200} \sim 1.3 \times 10^{15}\ M_{\odot}$; Munari et al. 2014) at a redshift of 0.09 (Owers et al. 2011). The cluster hosts a moderate cool core ($K_0 = 68$ keV cm^2; Cavagnolo et al. 2009) and exhibits multiple concentric cold fronts in its central regions (Markevitch et al. 2000; Rossetti et al. 2013), which are indicative of ongoing sloshing activity extending out to 1 Mpc from the cluster center (Rossetti et al. 2013). The sloshing activity may have triggered the formation of an unusual radio halo (Farnsworth et al. 2013). Owers et al. (2011) studied the three-dimensional (3D) galaxy distribution out to ~2 Mpc from the cluster core and identified several substructures associated with minor mergers. Eckert et al. (2014) discovered an infalling galaxy group located ~1.5 Mpc northeast (NE) of the main cluster. This subcluster is in the process of being stripped from its hot gas by the ram pressure applied by the main cluster, forming a spectacular X-ray tail. On larger scales, A 2142 is located in the core of a collapsing supercluster (Einasto et al. 2015; Gramann et al. 2015). Together, these studies reveal that A 2142 is a dynamically active cluster located at a node of the cosmic web.

The paper is organized as follows. In Sect. 2 we describe the analysis of the X-ray data to obtain radial profiles of the surface-brightness, temperature, and metal abundance of A 2142. In Sect. 3, we perform a deprojection of the profiles of X-ray surface brightness and SZ y parameter from *Planck* assuming spherical symmetry to recover the 3D gas density and pressure profiles. In Sect. 4, we combine the resulting SZ pressure profile with the X-ray density profile to obtain radial profiles of entropy, temperature, hydrostatic mass, and gas fraction. We also estimate the effects of gas clumping by comparing the results obtained with the azimuthal median method with those obtained using the traditional approach. Our results are discussed in Sect. 5.

Throughout the paper, we assume a ΛCDM cosmology with $\Omega_\Lambda = 0.7$, $\Omega_m = 0.3$ and $H_0 = 70$ km s^{-1} Mpc^{-1}. At the redshift of A 2142, 1 arcmin corresponds to 102 kpc. Uncertainties throughout the paper are provided at the 1σ confidence level. We use as reference values for R_{200} and R_{500}, $R_{200} = 2160$ kpc, and $R_{500} = 1408$ kpc, which are the results of a joint analysis performed in Munari et al. (2014) based on kinematics, X-ray, and gravitational lensing observations of A 2142.

2. X-ray spectral analysis

2.1. Description of the XMM data

Abell 2142 was mapped by *XMM-Newton* through five pointings: a central one (50 ks) and four 25 ks offset pointings obtained in extended full frame mode for pn and full frame for MOS. The data were processed with the *XMM-Newton* Scientific Analysis System (XMMSAS) v13.0. using the Extended Source Analysis Software package (ESAS Snowden et al. 2008). We filtered out the time periods affected by soft proton flares using the tasks `MOS-filter` and `pn-filter` to obtain clean event files. In Table 1 we provide the OBSID and the clean exposure time of the pointings. Point sources were detected and masked down to a fixed flux threshold (10^{-14} erg/cm^{-2} s^{-1}) via the ESAS task `cheese`. The presence of anomalous MOS CCDs was also taken into account.

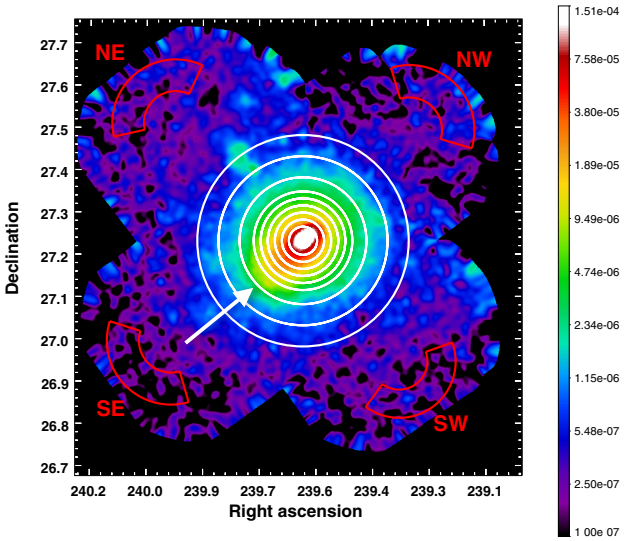

Fig. 1. Combined *XMM-Newton* mosaic in the energy band [0.7−1.2] keV corrected for the different exposure times and for the NXB. The units in the color bar are MOS count/s. The concentric white circles show the regions chosen for the source spectral extraction. The outermost circle has a radius of 15 arcmin (corresponding to ∼1530 kpc). The four regions delimited by the red curves were used to estimate the local sky background components. The labels represent the four regions used in the analysis: the northeast (NE), northwest (NW), southeast (SE), and southwest (SW) observations. The white arrow indicates the location of the outermost cold front (Rossetti et al. 2013, see Sect. 5.1.3). The tip of the accreting substructure observed in the region NE, as reported in Eckert et al. (2014), is located at approximatively (RA = 239.72°, Dec = 27.40°).

In Fig. 1 we show the combined EPIC mosaic of the cluster in the energy band [0.7−1.2] keV corrected for the exposure time for the three instruments (Eckert et al. 2014). Circular black areas in this image represent masked point sources.

2.2. Spectral analysis

We performed a spectral analysis in the [0.5−12] keV energy band of the cluster in the concentric regions shown in Fig. 1 and estimated the spectra of the local sky background components from the regions in the four red sectors in the same energy band. These regions are located at a distance of 28 arcmin from the cluster center, where we see no evidence for cluster emission. Spectra and response files were extracted using the ESAS tasks `MOS-spectra` and `pn-spectra`. For each of the annuli for which it was possible, we combined the different observations (center, NE, SE, SW, NW, see Fig. 1) in the spectral analysis.

The modeling of the background and of the source is described in Sects. 2.2.1 and 2.2.2, respectively. The fitting procedure was performed using XSPEC v12.7.1.

2.2.1. Background modeling

As shown in a number of recent studies (e.g., Leccardi & Molendi 2008; Ettori & Molendi 2011), the modeling of the background is critical to obtain reliable measurements of the properties of the ICM in cluster outskirts. The total background is made of two main components: the sky background and the non-X-ray background (NXB). The procedure adopted here to model these components follows Eckert et al. (2014) and is described in the following.

– The sky background can be modeled with three components: the cosmic X-ray background (CXB), the Galactic halo, and the local hot bubble. The emission of the CXB can be described by a power law with a photon index fixed to 1.46 (De Luca & Molendi 2004). This component is absorbed by the Galactic column density along the line of sight. We used a hydrogen column density of 3.8×10^{20} cm^{-2} in this analysis as measured from the LAB HI Galactic survey (Kalberla et al. 2005). The emission of the Galactic halo can be represented by a thermal component at a temperature of 0.22 keV (McCammon et al. 2002). We modeled this thermal emission with the thin plasma model APEC (Smith et al. 2001), with solar abundance. This emission is also affected by absorption along the line of sight. The local hot bubble is modeled with an unabsorbed thermal component at 0.11 keV. We used the APEC model to represent this thermal component, again with solar abundance. The normalization of these components was fit to each background region independently and then rescaled to the area of the region used for the spectral extraction. For these three background components, we only allowed the normalization to vary.
– The second source of background, the NXB, is induced by charged particles interacting within the detector. It is dominated by cosmic rays, i.e., relativistic charged particles that hit and excite the detector. Fluorescence emission lines are then emitted once the atoms of the detector de-excite. The spectrum of this background contribution can be estimated from the spectrum obtained during closed-filter observations using the method outlined in Snowden et al. (2008). A model of the NXB for all three EPIC detectors (pn, MOS1, and MOS2) was extracted from filter-wheel-closed data using the ESAS procedures `MOS-spectra` and `pn-spectra`. For each observation, we rescaled these spectra by comparing the count rates measured in the unexposed corners of the detectors with the mean count rates of the closed-filter observations. The resulting closed-filter spectra can be characterized by a flat continuum with several fluorescence emission lines. For each considered region, we modeled these spectra with a phenomenological model consisting in a broken power law and several Gaussians and used the resulting fit as an appropriate model of the NXB.
A priori, soft protons could also affect the data. In Table 1, we show the IN/OUT ratio (De Luca & Molendi 2004; Leccardi & Molendi 2008), which is the ratio between the surface brightness in the FOV and the surface brightness in the unexposed corners (out the FOV) in the hard energy band. Since soft protons are focused by the telescope mirrors, while cosmic rays can induce X-ray emission over the entire detector, this ratio is used as an indicator of the contamination of the soft protons to the NXB background. We find that the contamination by soft protons is very low, except for the NW observation, where it reaches a level of 25%. Leccardi & Molendi (2008) estimated the effect of soft protons on the spectral fitting analysis and found that for regions that are bright enough ($R < R_{500}$) this contribution is subdominant. Given that we stop the spectral extraction at R_{500}, we decided to neglect the contribution of the soft protons in the spectral fitting procedure.
The Solar Wind Charge Exchange (SWCX; Carter & Sembay 2008; Carter et al. 2011) is also a potential source of background in X-ray observations of cluster outskirts. Given that SWCX emission is time variable, the consistency of the spectral fits of the sky components at different times in the four regions considered in our analysis (see Table 2)

Table 1. OBSID, clean exposure time and IN/OUT ratio for the five observations used in this paper.

Observation	OBSID	Total [ks]	pn [ks]	MOS1 [ks]	MOS2 [ks]	IN/OUT ratio
Center	0674560201	59.1	48.8	52.3	53.8	1.074
NW	0694440101	24.5	12.5	19.6	18.2	1.260
SE	0694440501	34.6	29.8	33.1	32.5	1.139
SW	0694440601	38.6	24.1	30.0	31.7	1.154
NE	0694440201	34.6	29.7	32.9	33.2	1.060

Table 2. Fit of the local sky background components (local hot bubble, LHB; Galactic halo, GH; and cosmic X-ray background, CXB) using the model *constant(apec + wabs(apec + powerlaw),* on the four regions delimited by the red sectors in Fig. 1.

	LHB norm	LHB Δnorm	GH norm	GH Δnorm	CXB norm	CXB Δnorm
NE	1.69	[1.29; 2.04]	1.20	[1.07; 1.30]	0.938	[0.878; 0.988]
NW	3.39	[2.71; 3.90]	1.11	[0.978; 1.30]	0.949	[0.832; 1.00]
SE	0.430	[0.181; 0.921]	1.36	[1.20; 1.42]	0.844	[0.770; 0.912]
SW	1.64	[1.13; 1.93]	1.34	[1.25; 1.48]	0.925	[0.832; 0.971]
ALL	1.53	[1.35; 1.81]	1.25	[1.21; 1.32]	0.896	[0.866; 0.931]

Notes. The name of the observation represents the considered region. ALL means that the four regions have been fitted simultaneously. Only the normalization parameters were allowed to vary in this model. Units are [10^{-6}/cm^{-5}] for the normalization of the local bubble and of the Galactic halo and [10^{-6} photons/(keV cm^2 s)] for the normalization of the CXB.

argues against an significant contamination by this component. Furthermore, the level of the solar proton flux detected with the Alpha Monitor (SWEPAM) instrument on board the Advanced Composition Explorer (ACE) satellite is below 4×10^8 protons/(s cm^2), which is typical of the quiescent Sun, and is not sufficient to trigger SWCX. Therefore, we neglect this background component in our spectral analysis.

We estimated the normalizations of the various components of the local sky background (CXB; Galactic halo and local bubble) and of the NXB from the combined analysis of the four regions delimited in red in Fig. 1. The results of the fits of the sky background components for each of the four observations separately and for the combined fit are provided in Table 2. To fit the spectrum of these regions, the intensity of the NXB fluorescence lines in the energy range 1.2−1.9 keV (and also in the 7−9 keV energy range for the pn instrument), as well as that of the continuum, were left free to vary. The normalization of the CXB was fitted locally to take cosmic variance into account, which is expected to be of the level of 15% (Moretti et al. 2003).

By the comparison of the result of the fit in the four regions, we note that the normalization of the local hot bubble is not well constrained by these measurements. This is easily explained by the low temperature of this component (0.11 keV), which is below the energy range covered by *XMM-Newton* EPIC (0.5−12 keV). This renders the overall model largely insensitive to this component, such that uncertainties in the local hot bubble normalization are not expected to affect the result of the present study.

2.2.2. The source emission

We extracted spectra from concentric annuli centered on the cluster (RA = 239.58°, Dec = 27.23°) as depicted in Fig. 1 by the white circles. In each annulus, we fitted the resulting spectra with the thin plasma emission code APEC and we derived projected radial profiles of emission measure, temperature, and metal abundance. The surface-brightness profile obtained from the normalization of the APEC thermal model and the temperature profile are shown in Figs. 2 and 3, respectively. The excellent data quality allowed us to extract the abundance profile up to 15 arcmin ($\sim R_{500}$). The resulting abundance profile is shown in Fig. 4 and exhibits a slightly decreasing behavior from $Z = 0.35\ Z_\odot$ in the core down to $\sim$0.15 $Z_\odot$ at R_{500}, where $Z_\odot$ represents the solar abundance (Anders & Grevesse 1989). The best-fit temperature and normalization are relatively unaffected by the metal abundance even in the outermost bins. Indeed, fixing the metal abundance to 0.25 $Z_\odot$ instead of leaving it free to vary does not change the output parameters. For completeness, we also show the two-dimensional spectroscopic temperature profile obtained by *Suzaku* (Akamatsu et al. 2011) in Fig. 3. The temperatures measured by *Suzaku* significantly exceed those obtained in our analysis in the central regions, however, the temperature profile derived by Akamatsu et al. (2011) was extracted only along the NW, while that obtained in our analysis is azimuthally averaged. The spectroscopic temperature profile extracted with *XMM-Newton* in the NW direction agrees with the profile of Akamatsu et al. (2011, see Fig. D.2), which shows that the difference is caused by genuinely higher temperatures in the NW direction rather than by systematic differences between the two instruments. This conclusion is reinforced by independent observations performed with Chandra (see the temperature map in the work of Owers et al. 2009), which also indicate an increase of the temperature in the NW direction.

The best-fit values for the parameters are listed in Table 3. For the outermost three annuli (7−9, 9−12, and 12−15 arcmin), we performed a combined fit of the different observations (NE, NW, SW, SE, and center, as defined in Fig. 1). To do so, we fixed the sky background components of each observation to the values obtained in the previous section (see Table 2) and rescaled them by the ratio of the source area to the background area.

The parameter values shown in Table 3 are the results of the combined fit. The results of the fit performed in each region separately are listed in Tables D.1−D.3. We did not include the NE region in the combined fit of the annulus 7−9 arcmin or the central region in the combined fit of the annulus 12−15 arcmin, because the areas of overlap were too small to be included in the analysis.

Table 3. Fit of the *XMM-Newton* spectra with an APEC model in the regions delimited by the concentric white circles in Fig. 1.

R(arcmin)	T	ΔT	Norm	Δnorm	Z	ΔZ
0–0.3	6.26	[6.12, 6.37]	7.67	[7.60, 7.71]	0.321	[0.295, 0.350]
0.3–0.6	6.19	[6.10, 6.28]	6.38	[6.33, 6.41]	0.319	[0.301, 0.342]
0.6–1	6.68	[6.61, 6.75]	3.92	[3.90, 3.93]	0.293	[0.278, 0.310]
1–2	7.34	[7.27, 7.43]	1.82	[1.81, 1.82]	0.252	[0.240, 0.264]
2–3	7.93	[7.86, 8.03]	7.38×10^{-1}	$[7.34 \times 10^{-1}, 7.40 \times 10^{-1}]$	0.277	[0.263, 0.294]
3–4	8.15	[8.02, 8.24]	3.77×10^{-1}	$[3.75 \times 10^{-1}, 3.78 \times 10^{-1}]$	0.221	[0.203, 0.239]
4–5	8.15	[8.03, 8.29]	2.34×10^{-1}	$[2.33 \times 10^{-1}, 2.36 \times 10^{-1}]$	0.244	[0.223, 0.267]
5–6	7.89	[7.70, 8.10]	1.53×10^{-1}	$[1.52 \times 10^{-1}, 1.54 \times 10^{-1}]$	0.248	[0.224, 0.279]
6–7	7.86	[7.65, 8.15]	9.98×10^{-2}	$[9.90 \times 10^{-2}, 1.01 \times 10^{-1}]$	0.266	[0.226, 0.307]
7–9	7.30	[7.10, 7.49]	5.77×10^{-2}	$[5.72 \times 10^{-2}, 5.81 \times 10^{-2}]$	0.320	[0.290, 0.352]
9–12	7.09	[6.71, 7.36]	2.23×10^{-2}	$[2.21 \times 10^{-2}, 2.25 \times 10^{-2}]$	0.182	[0.140, 0.225]
12–15	4.75	[4.36, 5.13]	8.34×10^{-3}	$[8.12 \times 10^{-3}, 8.57 \times 10^{-3}]$	0.174	[0.102, 0.252]

Notes. The free parameters of the model are the temperature (in keV), norm (in 10^{-3} cm^{-5}), and abundance (in solar metallicity). For the outermost three radial bins, all the available observations were combined. For details, see text and Tables D.1–D.3 for the results of the individual fits.

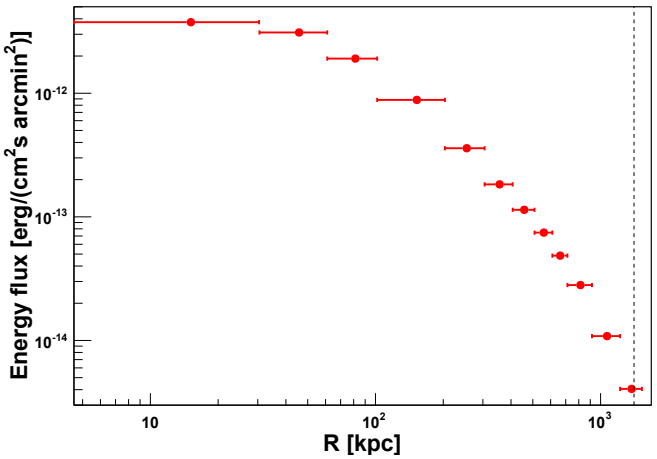

Fig. 2. Surface-brightness profile obtained by spectral fitting of the regions shown in Fig. 1. The dashed line represents the location of R_{500}.

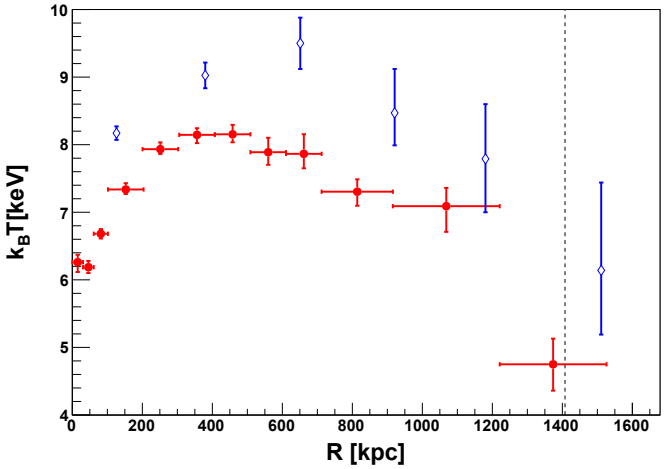

Fig. 3. Temperature profile. Red: *XMM-Newton* measurements for the regions shown in Fig. 1. Blue: *Suzaku* results (from Akamatsu et al. 2011). The dashed line represents the value of R_{500}.

3. X-ray and SZ imaging analysis

3.1. X-ray surface-brightness profile

Because of the faint cluster emission and the relatively high background of *XMM-Newton*, spectroscopic measurements beyond $\sim R_{500}$ are affected by systematic uncertainties (Leccardi & Molendi 2008; Ettori & Molendi 2011). For this reason, we adopted a different approach that allows us to extract surface-brightness profiles with much poorer signal-to-noise than spectroscopic profiles and, therefore, out to R_{200} and beyond (see Appendix B). We refer to this surface-brightness profile as photometric in the following, to be distinguished from the spatially limited spectroscopic surface-brightness profile.

We extracted photon images in the energy band [0.7–1.2] keV and created exposure maps for each instrument via the SAS task `eexpmap` and the `PROFFIT` v1.2 software (Eckert et al. 2011) to obtain the photometric surface-brightness profile. The choice of the [0.7–1.2] keV band is motivated by the fact that this particular band maximizes the signal-to-noise ratio (Ettori et al. 2010; Ettori & Molendi 2011) and avoids the bright and variable Al Kα and Si Kα fluorescence lines without affecting the statistics too much. Surface-brightness profiles were accumulated in concentric annuli starting from the surface-brightness peak (RA = 239.58°, Dec = 27.23°), taking vignetting effects into account. We accumulated NXB profiles in the same regions from the NXB maps, taking both the contribution of the quiescent particle background and the soft protons into account. To model the contamination from residual soft protons, we extracted the spectra of the entire observations and fitted the high-energy part of the spectra (7.5–12 keV) using a broken power-law model (see Leccardi & Molendi 2008). A 2D model for the contamination of residual soft protons was created using the ESAS task `proton` following Kuntz & Snowden (2008). The details of the soft-proton modeling technique are provided in Appendix A, and a careful validation using blank-sky pointings is presented in Appendix B together with an assessment of systematic uncertainties.

In addition, we also derived the azimuthal median surface-brightness profile following the method described in Eckert et al. (2015). Namely, Voronoi tessellation was applied on the count image to create an adaptively binned surface-brightness map with a minimum of 20 counts per bin. The median surface brightness was then estimated in each annulus by weighting the surface brightness of each bin by its respective surface. To estimate the uncertainty in the median, we performed 10^4 bootstrap

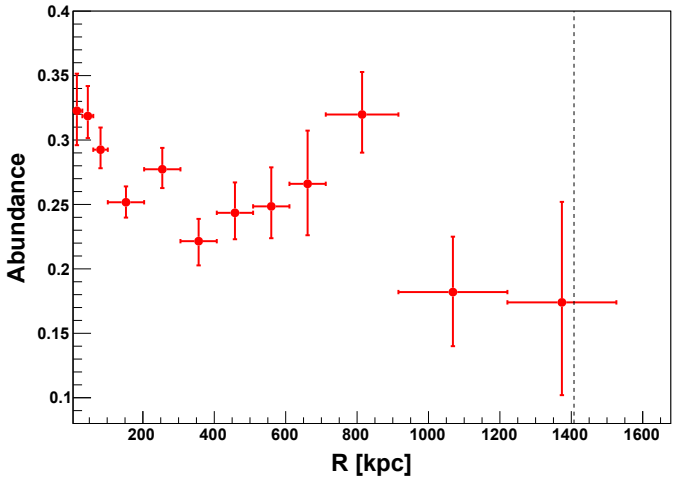

Fig. 4. Metal abundance profile for the regions shown in Fig. 1. The dashed line indicates the location of R_{500}.

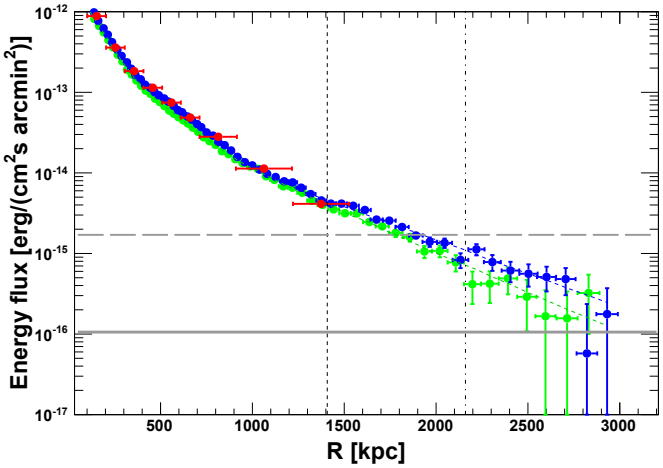

Fig. 5. Surface-brightness profiles of A 2142 obtained with different methods. The data points show the spectroscopic measurements (red), the azimuthally averaged profile (blue), and the azimuthal median (green). The green and blue thin dashed lines show the corresponding best fits obtained with the multiscale deprojection method. The solid and dashed horizontal lines correspond to the total background level and to the uncertainty on the background, respectively. The dashed and dash-dotted vertical lines represent R_{500} and R_{200}, respectively.

resampling of the surface-brightness distributions binned uniformly using Voronoi tessellation. The standard deviation of the bootstrap realizations was then adopted as the error on the median. In the [0.7−1.2] keV energy band, the systematic uncertainty in the subtraction of the background amounts to 5% of the sky background component, as shown by an analysis of a set of 22 blank-sky pointings (see Appendix B). This uncertainty was added in quadrature to the surface-brightness profiles. To convert the resulting surface-brightness profiles into emission measure, we folded the APEC model through the *XMM-Newton* response and computed the conversion between count rate and emission measure. The conversion factor is roughly independent of the temperature in the energy band [0.7−1.2] keV, provided that the temperature does not fall below ∼1.5 keV.

In Fig. 5 we show the comparison between the spectroscopic and photometric surface-brightness profiles. An excellent agreement is found between the profiles obtained with the two methods. We can see that *XMM-Newton* detects a significant emission out to almost 3 Mpc from the cluster core, which corresponds to the virial radius $R_{100} \sim 2 \times R_{500}$.

3.2. XMM-Newton deprojected electron density profile

The normalization of the APEC model, in units of cm^{-5}, is related to the electron density (n_e) by

$$\mathrm{Norm} = \frac{10^{-14}}{((1+z)\cdot D_a)^2} \int n_e n_p \mathrm{d}^3 r, \quad (1)$$

where $D_a \sim 349.8$ Mpc is the angular distance to the cluster in cm, $z = 0.09$ is its redshift, and n_p is the proton density (in cm^{-3}), which is related to the electron density by $n_e = 1.21 n_p$, assuming that the plasma is fully ionized.

After having converted the surface-brightness profile into emission measure, we deprojected the resulting profiles to estimate the 3D electron density profile. For the deprojection, we compared the output of two different methods: the multiscale method described in Eckert et al. (2016) and an onion-peeling method (Ettori et al. 2010). Both methods assume spherical symmetry. The differences between the output of the two procedures thus gives us a handle on the uncertainties associated with the deprojection.

In the multiscale deprojection method, the projected profile is decomposed into a sum of multiscale basis functions. Each component can then be easily deprojected to reconstruct the 3D profile. Following Eckert et al. (2016), we decompose the projected profile into a sum of King profiles, with s the projected radius, related to the line-of-sight distance and the 3D radius r, by $r^2 = s^2 + \ell^2$,

$$EM(s) = \sum_{i=1}^{N} N_i \left[1 + \left(\frac{s}{r_{c,i}}\right)^2\right]^{-3\beta_i/2}, \quad (2)$$

where i represents the ith basis function and s the projected radius. The parameters of this fit are the normalization (N_i), core radii ($r_{c,i}$), and slopes (β_i). The number of components and core radii used for the fit of the projected profile are determined adaptively from the total number of data points with the condition that one basis function is used for each block of four data points. The relation between the projected and 3D profiles can then be computed analytically (see Appendix A of Eckert et al. 2016, for details). This method provides an adequate representation of the observed profile and underlying density 3D profile, although the derived parameters have no actual physical meaning. The confidence intervals are derived using the Markov chain Monte Carlo (MCMC) code `emcee` (Foreman-Mackey et al. 2013). In the following, all chains have a burn-in length of 5000 steps and contain 10 000 steps. Chains are started from the best-fit parameters. All reported errors correspond to 68% confidence interval around the median of the MCMC distribution.

As an alternative, we used a direct nonparametric geometrical deprojection method based on the method of Fabian et al. (1981, see also Kriss et al. 1983; McLaughlin 1999; Buote 2000). The observed surface-brightness profile is considered the sum along the line of sight of the gas emissivity weighted by the fraction of the shell volume sampled in the given annular ring. From the outermost radial bin, and moving inward with the onion-peeling method, the gas emissivity (and density) is recovered in each shell. To avoid unphysical solutions induced by sharp fluctuations in the surface-brightness profile, the radial points that deviate more than 2σ from the median-smoothed profile are replaced by the corresponding values of the

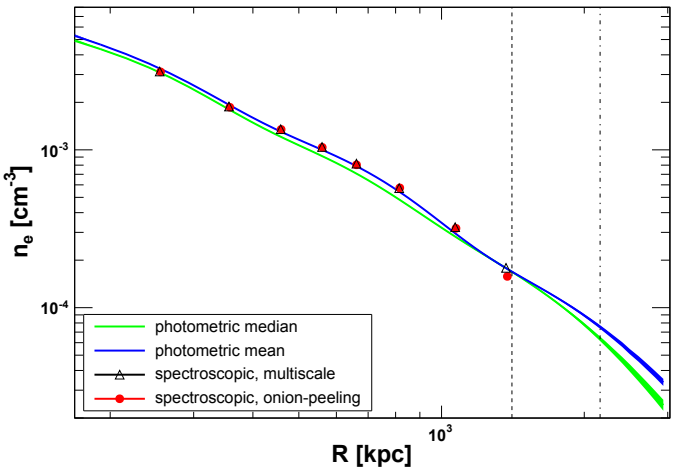

Fig. 6. Electron density profile. The data points show the deprojected spectroscopic data (from Table 3) using the multiscale method (black triangle; Eckert et al. 2016) and the onion peeling method (red dot; Ettori et al. 2010). The green and blue data curves show the density profiles recovered using the azimuthal median and azimuthal mean photometric surface-brightness profiles, respectively. Both profiles were deprojected using the multiscale method. The dashed and dash-dotted vertical lines represent R_{500} and R_{200}, respectively.

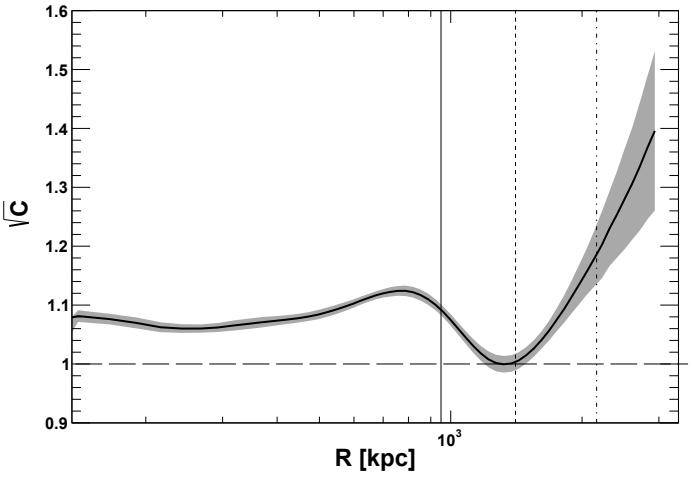

Fig. 7. Clumping factor profile. Solid line: median of the MCMC simulation; shaded area: 68% confidence interval around the median. The dashed and dash-dotted vertical lines represent R_{500} and R_{200}, respectively. The triple dot-dashed line shows the approximative position of maximal radius of the sloshing region reported in Rossetti et al. (2013).

median-smoothed profile. In the present case, only 2 (out of 64) data points have been replaced. The error bars are estimated from the distribution of the deprojected values of the 100 Monte Carlo realizations of the X-ray surface-brightness profile.

The density profiles obtained with these two methods for the spectroscopic surface brightness are shown in Fig. 6. They are in excellent agreement. In this figure, we also compared these spectroscopic profiles to the azimuthal mean and azimuthal median density profiles obtained from the photometric analysis (Sect. 3.1). We calculated both photometric profiles using the multiscale deprojection method. Hereafter, we adopt the multiscale deprojection method to provide the gas density profiles of reference. As expected, the spectroscopic data points are following the trend of the azimuthal mean density profile, and overestimate the density in each shell compared to the azimuthal median. The systematic difference is even more visible than in the APEC norm profiles (Fig. 5). This illustrates the potential bias induced by gas clumping when using the spectral fitting procedure.

3.3. Clumping factor profile

In X-rays, the measured emissivity provides information on $\langle n_e^2 \rangle$, where $\langle \cdot \rangle$ represents the mean inside spherical shells. The level of inhomogeneities in the ICM can be estimated by the clumping factor C, as $C = \langle n_e^2 \rangle / \langle n_e \rangle^2$ (Mathiesen et al. 1999).

This definition of the clumping factor reflects variations of the gas density in a given volume. Such variations are expected to be accompanied by variations of others thermodynamic properties. In the following, we exploit the fact that the X-ray volume emissivity in the energy range addressed in this work ([0.7−1.2] keV) is essentially independent of the gas temperature, which allows us to use the analysis based on the X-ray photometry as a direct proxy of the clumping factor.

Given that the density distribution inside a shell can be described by a lognormal distribution skewed with denser outliers, the median of the density distribution is robust against the presence of outliers, whereas the mean of the distribution overestimates the density inside the considered region (Zhuravleva et al. 2013; Eckert et al. 2015). Thus the ratio between the azimuthal mean and the azimuthal median density profiles (see Fig. 6) can be used as an estimator of the square root of the clumping factor profile.

The resulting clumping factor is shown in Fig. 7. Beyond R_{500}, we observe that the clumping factor increases with the distance to the cluster center, while at smaller radii, the clumping factor is roughly constant at the value $\sqrt{C} = 1.1$, followed by a decrease at about 1 Mpc from the cluster core. This behavior is discussed in detail in Sect. 5.1.

3.4. Planck deprojected electron pressure profile

To derive the electron pressure profile (P_e), we first need to estimate the thermal SZ signal from A 2142. The SZ effect provides a measurement of the thermal pressure integrated along the line of sight (through the dimensionless y parameter),

$$y(s) = \frac{\sigma_T}{m_e c^2} \int P_e(\ell) \mathrm{d}\ell, \tag{3}$$

where ℓ is the distance along the line of sight, σ_T the Thomson cross section, m_e the mass of the electron, and c the speed of light.

We make use of the all-sky survey from the *Planck* mission (Tauber et al. 2010; Planck Collaboration I 2016), and more specifically from the full survey data from the six frequency bands of the high frequency instrument (Lamarre et al. 2010; Planck HFI Core Team 2011). The SZ signal map was reconstructed over a patch map of 1024 × 1024 pixels^2 centered at the location of A 2142 and with a size of 20 × R_{500} (i.e., 4.6 degrees). We applied the Modified Internal Linear Combination Algorithm (MILCA; Hurier et al. 2013) to produce a map of the Comptonization parameter, y, in a tangential Galactic coordinates referential. This algorithm was also used to produce the full sky y map delivered by the Planck Collaboration to the community (Planck Collaboration XXI 2014; Planck Collaboration XXII 2016); MILCA offers the possibility to perform the SZ signal reconstruction in multiple bins of angular scales. As a consequence, we were able to produce a SZ map of A 2142 at 7 arcmin FWHM angular

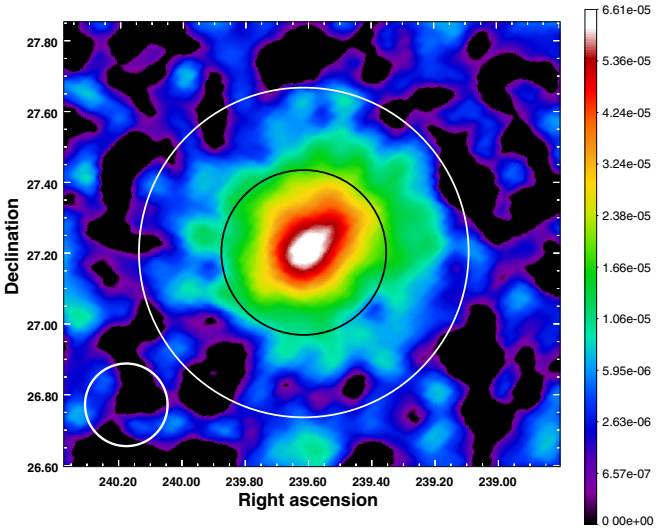

Fig. 8. *Planck* map of the Comptonization parameter, y, for A 2142. The black and white circles indicate the approximate location of R_{500} and $R_{100} \sim 2 \times R_{500}$, respectively. The white circle in the bottom left corner indicates the size of a 7 arcmin beam FWHM.

resolution. Our A 2142 SZ-map has therefore a significantly better resolution than the public full sky SZ-map at 10 arcmin FWHM. Thus, our SZ map uses the information from the 100 GHz Planck channel (roughly 10 arcmin FWHM) only for large angular scales (see Hurier et al. 2013, for a more detailed description of the procedure). The resulting y-map for A 2142 is shown in Fig. 8. A 2142 was very well detected as an SZ source in the *Planck* survey, with an overall signal-to-noise ratio of 28.4 (Planck Collaboration XXXII 2015; Planck Collaboration XXVII 2016). Owing to its extension over the sky A 2142 is among the clusters spatially resolved in the *Planck* survey through its SZ signal, which clearly extends well beyond R_{500} out to $R_{100} \sim 2 \times R_{500}$ (as shown in Fig. 8).

We further proceeded in extracting the y-parameter profile of A 2142 from our MILCA y-map following the exact same method developed by Planck Collaboration Int. V (2013). The y profile is extracted on a regular grid with bins of width $\Delta\theta/\theta_{500} = 0.2$. The local background offset is estimated from the area surrounding the cluster beyond $5 \times \theta_{500} = 69$ arcmin. The resulting profile is shown in Fig. 9 together with a fit to the data obtained with the multiscale method. For the fitting procedure, we take into account the covariance between the data points, which conveys the statistical properties of the noise of each *Planck* frequency band used to compute the y-map and the oversampling factor of our patch with respect to the 1.71 arcmin resolution element in the *Planck* `HEALPIX` map (Górski et al. 2005). In addition, the model was convolved with the PSF of the instrument, which we approximated as a Gaussian with a full width at half maximum (FWHM) of 7 arcmin. The residual between the best fit convolved with the PSF and the y parameter data is shown in the bottom panel of Fig. 9.

The best-fit y-parameter profile (shown in Fig. 9) was then converted into a 3D electron pressure profile using the multiscale deprojection method. For completeness, we also deprojected the y parameter data using the same methodology as the Planck Collaboration Int. V (2013). In the latter case, the underlying pressure profile was obtained from a real space deconvolution and deprojection regularization method adapted from Croston et al. (2006), assuming spherical symmetry for the cluster. The correlated errors were propagated from the covariance matrix of the y profile with a Monte Carlo procedure and led to the estimation of the covariance matrix of the pressure profile $P_e(r)$.

To compare the resulting SZ pressure profiles with that obtained from purely X-ray analysis, we estimated the 3D pressure profile from the spectroscopic X-ray measurements using the method outlined in Vikhlinin et al. (2006). In this method, the 3D temperature profile is assumed to be represented by a parametric form with a large number of free parameters,

$$T(r) = T_0 \frac{(r/r_{\rm cool})^{a_{\rm cool}} + T_{\rm min}/T_0}{(r/r_{\rm cool})^{a_{\rm cool}} + 1} \frac{(r/r_t)^{-a}}{(1 + (r/r_t)^b)^c/b)}. \quad (4)$$

This functional form was projected along the line of sight weighted by the 3D emissivity profile, and subsequently fit to the observed temperature profile described in Sect. 2.2.2. We then ran an MCMC to sample the parameter space and draw the 3D temperature profile. The 3D X-ray pressure profile was computed by combining the deprojected temperature with the electron density profile obtained from the spectral X-ray analysis (black points in Fig. 6).

In Fig. 10 we show all three pressure profiles: the two SZ pressure profiles obtained by the two different deprojection methods described above (method 1: multiscale method; method 2: same methodology as Planck Collaboration Int. V 2013) and the spectroscopic X-ray pressure profile. All three pressure profiles are consistent, although we note a slight excess of the X-ray pressure profile compared to the SZ pressure profile at a distance of 500 kpc from the cluster center. Given that the thermal SZ signal is less affected by clumping (e.g., Roncarelli et al. 2013), this observed difference can be explained by fluctuations in the X-ray signal (see the value of the clumping factor $\sqrt{C} \sim 1.1$ in this radial range in Fig. 7). Also, around R_{200} the two pressure profiles recovered from SZ observations are slightly different. This may be because the multiscale deprojection method smoothes the fluctuations to fit the data with a superposition of King profiles. In addition to that, the points on the deconvolved and deprojected profile obtained using the same method as in Planck Collaboration Int. V (2013) are correlated. However, the errors shown on this figure are only the square root of the diagonal of the covariance matrix. This fact likely biases a direct visual comparison. The observed discrepancy around R_{200} may therefore not be a physical effect. We come back to the excess in the purely X-ray pressure profile compared to the SZ profile in the discussion section.

Owing to the moderate resolution of the *Planck* satellite (translating into 7 arcmin on our y-map), we can not recover constraints on the SZ pressure profile from the y parameter measurements close to the cluster center. Therefore, we consider in the following only the radial range beyond 400 kpc (~4 arcmin), which is the radius beyond which the constraints on the pressure profile from the SZ data are less impacted by the PSF blurring and, therefore, more reliable.

4. Joint X-ray and SZ analysis

The combination of the X-ray and SZ signal can be used to recover the thermodynamical quantities that characterize the ICM. In this section, we combine the 3D SZ pressure profile with the X-ray gas density profile to recover the radial distribution of temperature, entropy, hydrostatic mass, and gas fraction. Moreover, we can recover these quantities, which are largely corrected for the effect of the clumped gas. This is obtained by comparing the X-ray surface brightness measured using the mean of

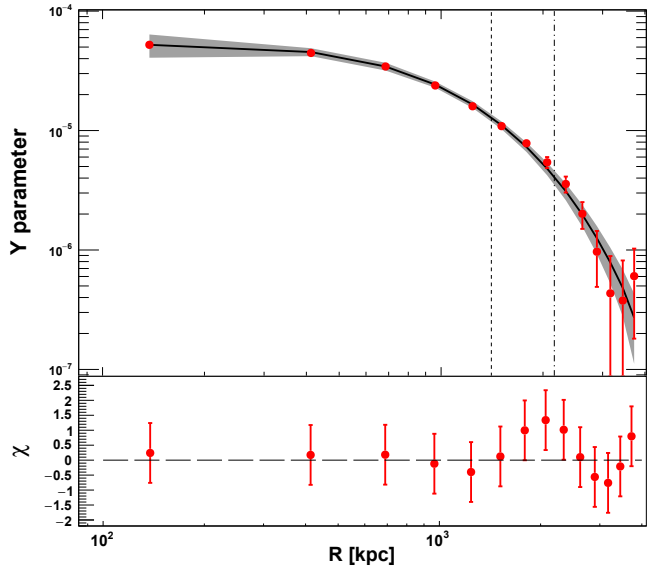

Fig. 9. *Top panel*: compton-y parameter profile from *Planck* data (red points). The gray solid line and shaded area show the best-fit profile convolved with the instrument PSF. The data points are correlated and the associated errors correspond to the square root of the diagonal elements of the covariance matrix. *Bottom panel*: residual of the fit to the *Planck* data. The dashed and dash-dotted vertical lines represent R_{500} and R_{200}, respectively.

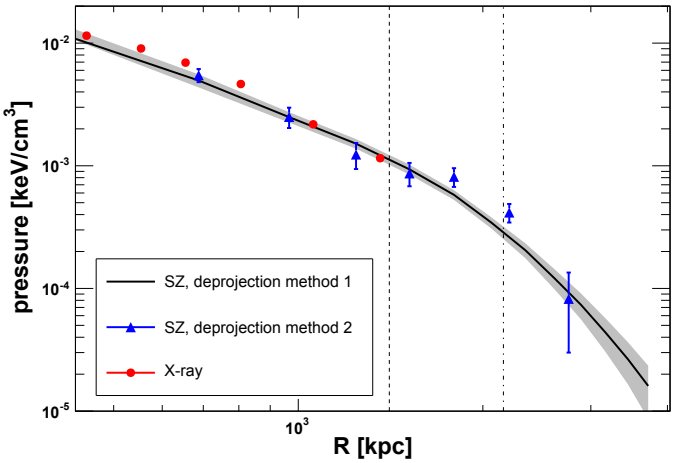

Fig. 10. Electron pressure profile. The gray solid line and shaded area show the best-fit pressure profile obtained by deprojecting the SZ data using the multiscale method (deprojection method 1). The red points show the spectroscopic X-ray data deprojected with the method of Vikhlinin et al. (2006) and the blue triangles show the result of the deprojection of the y parameter data using the same methodology as Planck Collaboration Int. V (2013) (deprojection method 2). The blue data points are correlated and the associated errors correspond to the square root of the diagonal elements of the covariance matrix. The dashed and dash-dotted vertical lines represent R_{500} and R_{200}, respectively.

the azimuthal photon counts distribution with the X-ray surface brightness estimated with the median of the distribution (as detailed in Eckert et al. 2015).

4.1. Temperature profile

Assuming that ICM is an ideal gas, the joint X-ray and SZ 3D temperature profile can be recovered by combining the X-ray density profiles obtained in Sect. 3.2 (Fig. 6) with the SZ pressure profile derived in Sect. 3.4 (Fig. 10). Using the equation $k_{\rm B}T = P_{\rm e}/n_{\rm e}$, we derived the 3D temperature profile for both the azimuthal mean and the azimuthal median density profiles. While the density profile obtained using the azimuthal median is corrected for the presence of clumps, the density profile obtained using the azimuthal mean is not.

The resulting joint X-ray and SZ 3D temperature profiles are shown in Fig. 11. The uncertainties in the temperature profile were estimated by combining the MCMC runs for the pressure and density. At each radius, the temperature and its uncertainty were drawn from the distribution of output temperature values. In this figure we also show the deprojected spectroscopic temperature profile obtained with the method of Ettori et al. (2010).

As expected, we observe different behaviors of the temperature profile depending on whether gas clumping is taken into account or not. Indeed, the increase in the clumping factor toward the outskirts (see Fig. 7) causes the temperature profile obtained from the azimuthal mean to steepen with cluster-centric distance compared to the profile estimated with the azimuthal median technique. We also note that the spectroscopic X-ray profile closely follows the X-ray and SZ profile obtained using the azimuthal median (except for the very last data point, but this is an artefact of the deprojection method). We come back to this point in the discussion section.

The effect of the overestimate the density has a clear signature in the temperature profile. Similar effects are also expected in the other thermodynamic quantities derived from the X-ray analysis.

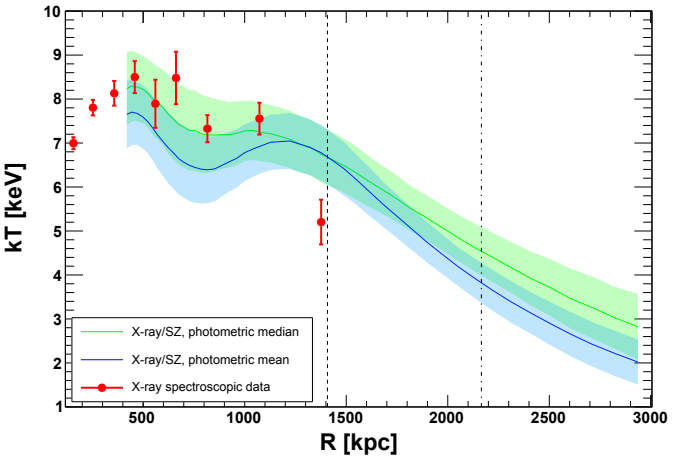

Fig. 11. Deprojected temperature profile. Red points: spectroscopic data (from Fig. 3) deprojected using the method of Ettori et al. (2010); green and blue: combined X-ray and SZ profile using the azimuthal median and azimuthal mean density profiles, respectively. The dashed and dash-dotted vertical lines represent R_{500} and R_{200}, respectively.

4.2. Entropy profile

Assuming that entropy is only generated by spherical virialization shocks driven by hierarchical structure formation, we expect an entropy profile that follows the gravitational collapse model. In such a case, the gas with low entropy sinks into the cluster center, while the high-entropy gas expands to the cluster outskirts (Voit et al. 2005; Pratt et al. 2010) and the resulting entropy profile has a power-law shape given by

$$K(R) = K_{500} \cdot 1.42 \left(\frac{R}{R_{500}}\right)^{1.1} \text{ keV cm}^2. \quad (5)$$

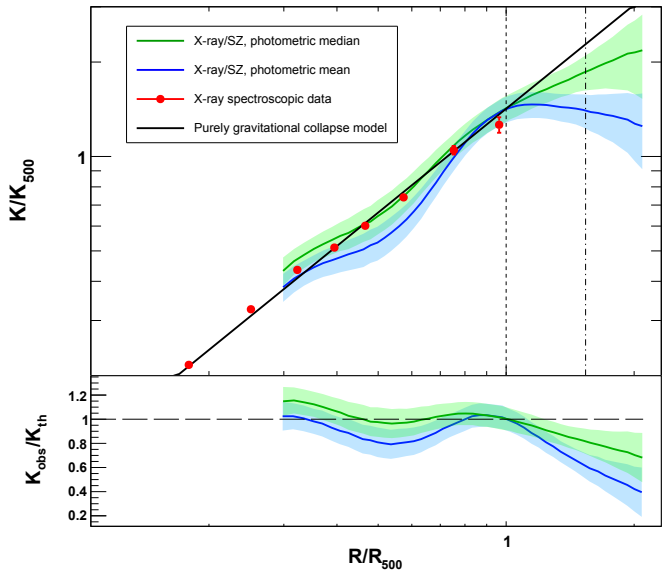

Fig. 12. Deprojected entropy profile. *Top panel*: the red dots show the X-ray spectroscopic data, while the green and blue curves represent the X-ray and SZ profiles obtained using the azimuthal median and azimuthal mean density profiles, respectively. The black line shows the expectation from purely gravitational collapse (Eq. (5), Voit et al. 2005). The dashed and dash-dotted vertical lines represent R_{500} and R_{200}, respectively. *Bottom panel*: ratio of the X-ray and SZ entropy profile ($K_{\rm obs}$) over the entropy profile expected from the purely gravitational collapse model ($K_{\rm th}$): for the azimuthal median (in blue) and azimuthal mean (in green) density profiles. The horizontal dashed line represents the expectation for $K_{\rm obs} = K_{\rm th}$.

The quantity K_{500} is defined as (Pratt et al. 2010)

$$K_{500} = 106 \cdot \left(\frac{M_{500}}{10^{14}\ M_{\odot}}\right)^{2/3} \left(\frac{1}{f_{\rm b}}\right)^{2/3} h(z)^{-2/3}\ \mathrm{keV\ cm^2}, \quad (6)$$

where $M_{500} = 8.66 \times 10^{14}\ M_{\odot}$ is the cluster mass at $R_{500} = 1408$ kpc (values derived from Munari et al. 2014), $f_{\rm b} = \Omega_{\rm b}/\Omega_{\rm m} = 0.15$ is the cosmic baryon fraction, where $\Omega_{\rm b}$ is the baryon density, $\Omega_{\rm m}$ is the matter density, and $h(z) = \sqrt{\Omega_{\rm m}(1+z)^3 + \Omega_{\Lambda}}$ the ratio of the Hubble constant at redshift z to its present value.

We derived the combined SZ and X-ray 3D entropy profile using the equation $K = P_{\rm e}/n_{\rm e}^{5/3}$ with the X-ray density profiles obtained in Sect. 3.2 (Fig. 6) and the SZ pressure profile derived in Sect. 3.4 (Fig. 10). In Fig. 12 we show the entropy profiles obtained using the azimuthal mean and median density profiles. For comparison, we also show the entropy profile obtained with the spectroscopic X-ray information ($K = k_{\rm B}T/n_{\rm e}^{2/3}$) from our deprojected temperature and gas density spectroscopic profiles. All profiles are rescaled by K_{500} and compared to the expectations of the self-similar model (Voit et al. 2005).

Excellent agreement is found between the X-SZ and spectroscopic X-ray profiles out to R_{500}.

At larger radii, the use of a method sensitive to outliers leads to an entropy profile that deviates from the self-similar prediction ($\propto R^{1.1}$) in the outskirts and produces a feature which resembles an entropy flattening.

On the contrary, we can see that the X-SZ profile obtained using the azimuthal median method rises steadily with radius out to the maximum radius accessible in this study (3000 kpc $\approx R_{100}$). Therefore, if the presence of clumps is taken into account in the X-ray data the deviation observed with the blue curve almost completely disappears and at R_{200} the entropy falls within just 1σ of the self-similar expectation.

We stress that the SZ effect is nearly insensitive to clumping (e.g., Battaglia et al. 2015), the difference between the two profiles is caused only by our treatment of gas clumping in the X-ray data. This shows the importance of taking the effects due to the presence of clumps in the derivation of the thermodynamics quantities into account.

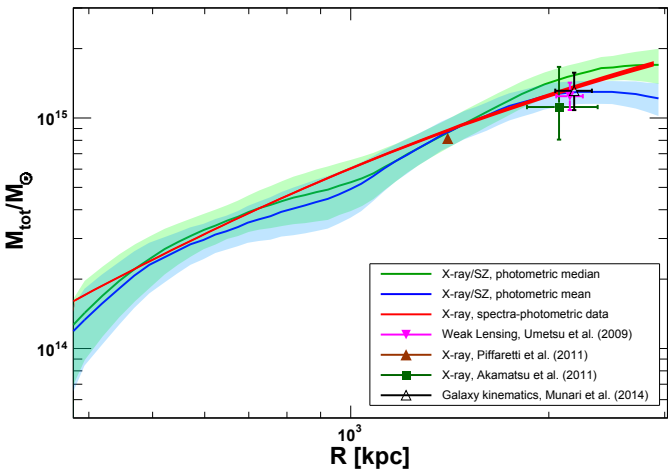

Fig. 13. Mass profile of A 2142. Green: X-SZ combined profile using the azimuthal median density profile. Blue: X-SZ combined profile using the azimuthal mean density profile. Red: NFW fit to the spectroscopic X-ray data using the method of Ettori et al. (2010). For comparison, we also plot the mass measurements reported in the literature. Brown triangle: M_{500} from $L_{\rm X} - M$ relation (Piffaretti et al. 2011); pink reversed triangle: M_{200} from Subaru weak lensing (Umetsu et al. 2009); dark green square: M_{200} from *Suzaku* X-ray (Akamatsu et al. 2011); black empty triangle: M_{200} from galaxy kinematics (Munari et al. 2014).

4.3. Hydrostatic mass

Assuming that the ICM is in hydrostatic equilibrium within the gravitational potential of the cluster, the total enclosed mass at the distance r from the cluster center can be estimated as

$$\frac{{\rm d}P_{\rm g}(r)}{{\rm d}r} = -\rho_{\rm g}(r)\frac{{\rm G}M_{\rm tot}(<r)}{r^2}, \quad (7)$$

where $P_{\rm g} = P_{\rm e} + P_{\rm p}$ is the gas pressure profile, $\rho_{\rm g} = (n_{\rm e} + n_{\rm p}) \cdot m_{\rm p}\mu$ is the gas mass density, where $m_{\rm p}$ is the mass of the proton, $\mu = 0.6$ the mean molecular weight, and G the universal gravitational constant.

Following Ameglio et al. (2009), we combined the *Planck* electron pressure profile (Sect. 3.4) with the *XMM-Newton* electron density profile (Sect. 3.2) to derive the hydrostatic mass profile. As above, we investigated the effect of clumping on the hydrostatic mass by comparing the results obtained with the azimuthal mean and median density profiles.

In Fig. 13 we show the combined X-ray and SZ hydrostatic mass profiles obtained for the different input density profiles. The mass profile obtained using the azimuthal median increases steadily, while the mass profile obtained with the azimuthal mean density profile shows an unphysical turnover at $R > R_{200}$. Such turnovers have been reported in the literature and interpreted as evidence for a significant nonthermal pressure contribution to sustain gravity (e.g., Kawaharada et al. 2010; Bonamente et al. 2013; Fusco-Femiano & Lapi 2014).

Table 4. M_{200} and R_{200} corresponding to the three hydrostatic mass profiles shown in Fig. 13 resulting from the combined X-ray and SZ or spectroscopic X-ray study.

	$M_{200}[10^{14}\ M_\odot]$	R_{200}[kpc]
X-SZ, median	16.1 ± 2.6	2347 ± 154
X-SZ, mean	12.9 ± 1.8	2179 ± 129
X-ray, spectroscopic+median	14.1 ± 0.3	2249 ± 16
X-ray, *Suzaku*	$11.1^{+5.5}_{-3.1}$	2080^{+300}_{-220}
Weak lensing	$12.4^{+1.8}_{-1.6}$	2160 ± 100
Kinematics	$13.1^{+2.6}_{-2.3}$	2190 ± 140

Notes. For comparison, we also list the values of M_{200} and R_{200} obtained from Subaru weak lensing (Umetsu et al. 2009), *Suzaku* X-ray (Akamatsu et al. 2011) and galaxy kinematics (Munari et al. 2014).

We also derived the hydrostatic mass profile using X-ray-only information with the method described in Ettori et al. (2010). This method assumes a Navarro-Frenk-White (NFW) form for the underlying mass profile and uses the deprojected gas density profile to reproduce the observed temperature profile estimated with the spectral analysis by inversion of the hydrostatic equilibrium equation applied on a spherically symmetric object. The best fit on the two parameters describing the NFW mass model, i.e., the concentration and R_{200} in the present analysis, is then obtained using a χ^2 minimization technique. Applying this method to the photometric median density profile, we measure a concentration $c = 3.00 \pm 0.06$ and $R_{200} = 2249 \pm 16$ kpc. Hereafter, all references to the method of Ettori et al. (2010) are applied to the photometric median density profile.

In Fig. 13 we compare the resulting mass profile with that obtained using the X-SZ method. We can see that the two methods lead to consistent results. Good agreement is found in particular between the X-ray-only and the median X-SZ profiles. We also show the comparison of several mass measurements from the literature: Akamatsu et al. (*Suzaku*, assuming hydrostatic equilibrium, 2011); Umetsu et al. (Subaru, weak gravitational lensing, 2009); Munari et al. (optical spectroscopy, galaxy dynamics, 2014); and Piffaretti et al. (ROSAT, $L_X - M$ relation, 2011). These measurements are summarized in Table 4. All our mass measurements are consistent within the error bars with the mass measurements made in Akamatsu et al. (2011), Umetsu et al. (2009), Munari et al. (2014), and Piffaretti et al. (2011).

4.4. Gas fraction profile

Because of their deep gravitational well, massive clusters are expected to retain the matter collected since their formation. Thus, the relative amount of baryonic and dark matter should be close to the universal value. Recent *Planck* observations of the power spectrum of CMB anisotropies indicate a universal baryon fraction $\Omega_b/\Omega_m = 0.153 \pm 0.003$ (Planck Collaboration XIII 2016). Corrected for the stellar fraction, which accounts for 10−20% of the total amount of baryons in galaxy clusters (e.g., Gonzalez et al. 2007), we expect a gas fraction of 13−14%.

Assuming spherical symmetry, the total gas mass is given by the integral of the gas density over the cluster volume,

$$M_{\rm gas}(<r) = 4\pi \int_0^r \rho_{\rm g}(r') r'^2 {\rm d}r', \quad (8)$$

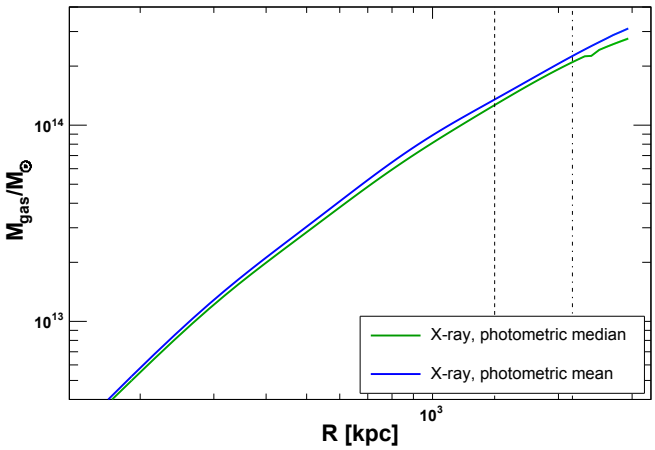

Fig. 14. Gas mass profiles obtained with Eq. (8). Green: using the azimuthal median density profile (green curve in Fig. 6). Blue: using the azimuthal mean density profile (blue curve in Fig. 6). The dashed and dash-dotted vertical lines represent R_{500} and R_{200}, respectively.

where ρ_g is defined as in Eq. (7). In Fig. 14 we show the resulting $M_{\rm gas}$ profiles obtained for the azimuthal mean and azimuthal median density profiles (see Fig. 6). We obtain consistent results within few percent via the method of Ettori et al. (2010). As expected, the $M_{\rm gas}$ profile resulting from the use of the azimuthal median density profile lies slightly below the profile obtained from the azimuthal mean. At R_{200}, the difference between the azimuthal median and azimuthal mean profiles is on the order of 6%.

We derived the gas fraction as a function of radius by combining the gas mass profiles with the corresponding hydrostatic mass profiles (see Sect. 4.3). In Fig. 15 we compare the resulting gas fraction profiles with the expected universal baryon fraction from *Planck*, which is corrected for the baryon fraction in the form of stars (Gonzalez et al. 2007). Interestingly, we can see that while the gas fraction profile derived from the combination of the azimuthal median density profile with the SZ pressure profile is almost constant and close to the expected value (∼13−14%), the gas fraction profile derived using the azimuthal mean density profile and the SZ pressure profile increases with radius and exceeds the cosmic baryon fraction. We also note that the gas fraction profile obtained from purely X-ray information is slightly above the expected value. We discuss these points further in Sect. 5.3.2.

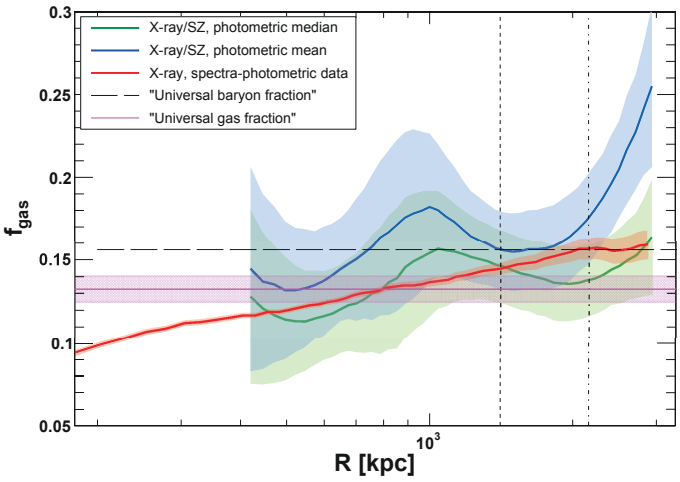

Fig. 15. Gas fraction profile. Green: X-SZ combined profile using the azimuthal median density profile. Blue: X-SZ combined profile using the azimuthal mean density profile. Red: NFW fit to the spectroscopic X-ray data using the method of Ettori et al. (2010). The dashed and dash-dotted vertical lines represent R_{500} and R_{200}, respectively. The dashed horizontal line represents the universal baryon fraction from *Planck* (Planck Collaboration XIII 2016), whereas the criss-crossed area shows the expected gas fraction corrected for the fraction of baryons in the form of stars (Gonzalez et al. 2007).

5. Discussion

The combination between deep X-ray and SZ data presented allowed us to extend the measurements of the thermodynamic properties of the ICM out to $2 \times R_{500} \sim R_{100}$, which corresponds roughly to the virial radius of the cluster. This is the first study in which we are able to estimate the effects of gas clumping and nonthermal energy self-consistently. Here we discuss our main results and their implications.

5.1. Gas clumping

5.1.1. The clumping factor beyond R_{500}

We estimated the effects of gas clumping on the gas density of the cluster by applying the azimuthal median method presented in Eckert et al. (2015). This method allows us to resolve all the clumps whose sizes exceed the size of the Voronoi bins, which given the depth of our *XMM-Newton* observation corresponds to scales of ~20 kpc around R_{200}, and to remove them from our analysis. On the other hand, in the spectroscopic analysis, the total number of detected photons is used, which leads to an overestimate of the surface brightness in the presence of inhomogeneities. This is illustrated in Fig. 6, where we can see that the gas density estimated using the spectroscopic analysis closely follows the results obtained with the azimuthal mean, but overestimates the azimuthal median. This shows that the azimuthal median is a more reliable estimator of the mean gas density, especially when studying the outskirts of galaxy clusters.

At R_{200}, we measured $\sqrt{C} = 1.18 \pm 0.06$, which is consistent with the value $\sqrt{C} = 1.25^{+0.31}_{-0.21}$ estimated by Eckert et al. (2015) using lower resolution ROSAT PSPC data. Because of projection effects, however, the method used here is only expected to provide an accurate measurement of the clumping factor when averaging over a sufficiently large number of clusters.

The relatively mild clumping factor estimated here is somewhat lower (albeit consistent) with the value $\sqrt{C} \sim 1.5$ measured by Morandi et al. (2013) from the dispersion of the surface-brightness distribution and with the value $\sqrt{C} \sim 1.4$ expected by Urban et al. (2014) to reconcile the measured entropy profile of the Perseus cluster with the expectation from pure gravitational collapse. Numerical simulations (see, e.g., Nagai & Lau 2011; Zhuravleva et al. 2013; Vazza et al. 2013) consistently predict a mean value $\sqrt{C} \sim 1.4$ around R_{200}, albeit with a rather large cluster-to-cluster scatter. Moreover, the exact value of the clumping factor was found to depend significantly on the adopted baryonic physics (Nagai & Lau 2011; Roncarelli et al. 2013). Indeed, gas cooling removes the most structured phase of the gas from X-ray-emitting temperatures, which results in a smoother gas distribution and a lower clumping factor, $\sqrt{C} \sim 1.2$ (Nagai & Lau 2011). Our measurements are therefore in better agreement with simulations that include additional physics.

5.1.2. Origin of the clumping

An important question to ask is whether the mild, but significant level of clumping observed in this study originates mainly from a population of compact infalling clumps or from large-scale asymmetries in the gas distribution, for example, coinciding with intergalactic filaments. In a recent paper, Roncarelli et al. (2013) divided the clumping effect into the contribution of individual infalling clumps and that of smooth, large-scale accretion patterns. While the former component strongly depends on the adopted baryonic setup, the latter (called the *residual clumping* C_R) is robust against the implementation of additional physical effects. To investigate whether the clumping observed here is caused mainly by a large population of small accreting clumps or by smooth, large-scale accretion patterns, following Roncarelli et al. (2013) we estimated the level of residual clumping C_R in our observing. To this aim, we computed the surface-brightness profile in 12 sectors of constant opening angle and computed the scatter of the surface-brightness values as a function of cluster-centric radius (Vazza et al. 2011). The azimuthal scatter can then be related to the residual clumping using the recipe described in Roncarelli et al. (2013), allowing us to assess the level of clumping induced, on average, by large-scale asymmetries.

In Fig. 16 we compare the total clumping from Fig. 7 with the residual clumping as a function of radius. We can see that our measurement of the clumping factor consistently exceeds the residual clumping with the exception of a small region around R_{500}. This shows that large-scale asymmetries account for a part, but not the entirety of the measured effect. At R_{200}, the residual clumping is roughly half of the total clumping, which reveals the presence of a population of small-scale clumps in the outskirts of the clusters (such as the accreting group, Eckert et al. 2014). The residual clumping, however, is obtained on average as representative of the simulated dataset.

5.1.3. The sloshing region

In addition to the increase in the clumping factor beyond R_{500}, we also noticed a slight excess in the clumping factor in the inner regions followed by a decrease at about 1 Mpc. This can be explained by the large-scale sloshing phenomenon taking place in A 2142 (Rossetti et al. 2013). Indeed, as pointed out in Rossetti et al. (2013), A 2142 exhibits three concentric cold fronts distributed along the main axis of the cluster (NW-SE), the largest of which is located nearly 1 Mpc SE of the cluster. The presence of this substructure is indicated in Fig. 1. The sloshing phenomenon induces alternating surface-brightness excesses

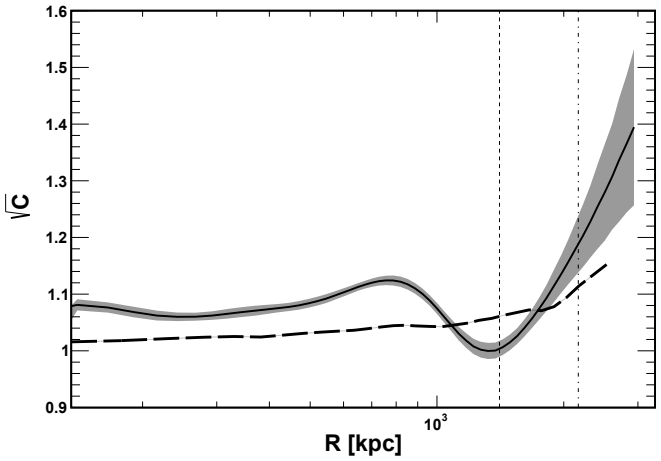

Fig. 16. Clumping factor estimated using the azimuthal median method (same as Fig. 7, solid line and shaded area) compared to the residual clumping (see text for details; dashed line, Roncarelli et al. 2013).

which, in turn, bias the mean surface-brightness high. On the other hand, the azimuthal median technique allows us to filter out the regions where the excess surface brightness is observed, leading to a lower estimate of the gas density. This example nicely illustrates the effectiveness of the azimuthal median technique in returning the surface brightness associated with the bulk of the ICM.

5.2. Thermodynamic properties

As discussed above, the main advantage of our analysis compared to previous works is that we are able to disentangle non-gravitational and clumping effects. Here we discuss the thermodynamic properties out to the virial radius measured in this work.

5.2.1. Temperature and pressure

The comparison between the pressure profiles obtained from spectroscopic X-ray and SZ analysis indicates excellent agreement between the results obtained with the two methods, as shown in Fig. 10. This shows that X-ray and SZ observations provide a very consistent picture of the state of the ICM, as already pointed out in detailed comparisons of the pressure profiles derived with the two methods (Planck Collaboration Int. V 2013; Sayers et al. 2013). Interestingly, we note a slight excess in the X-ray spectroscopic pressure profile around ~500 kpc. Given that the SZ effect is less sensitive to clumping, this excess can be explained by the overestimated gas density in the sloshing region (see above).

Given that the X-ray pressure profile is obtained by the product of the spectroscopic density profile with the spectroscopic temperature profile, this observed excess in the X-ray pressure profile implies that the spectroscopic temperature profile is less affected by clumping than the spectroscopic density profile. Otherwise, the two effects would balance and the X-ray pressure profile would tend to reproduce the features of the SZ pressure profile, which is less sensitive to clumping. Such an effect was also noticed by Rozo et al. (2012) in an analysis of *Chandra* versus *Planck* data and in Planck Collaboration Int. I (2012) in an analysis of *XMM-Newton* versus *Planck* data. In both studies, the authors studied the scaling relations between Y_{SZ} and Y_X, where Y_{SZ} is related to the total pressure within the cluster's volume and $Y_X = M_{gas}T$, its X-ray analog, and they concluded that Y_X was always in excess compared to Y_{SZ}.

A similar effect can be seen when comparing the spectroscopic X-ray temperature with the temperature estimated by combining SZ and X-ray imaging data (see Fig. 11). Namely, the temperature profile obtained when combining the SZ pressure profile with the azimuthal mean density profile systematically underestimates the spectroscopic X-ray temperature, while the clumping-corrected profile leads to a temperature in agreement with the spectroscopic data. Interestingly, the agreement between spectroscopic X-ray and clumping-corrected X-SZ temperatures is contrary to the expectations of Rasia et al. (2014), which predict that inhomogeneities in the density distribution should bias the observed spectroscopic temperature by 10 to 15%, and is in contradiction with the results of Mazzotta et al. (2004), who demonstrated based on numerical hydrodynamical N-body simulations that the projected spectroscopic temperature is lower than the emission-weighted temperature in the presence of inhomogeneities in the ICM. Conversely, our results are consistent with Frank et al. (2013), who studied the temperature distribution in a large cluster sample and pointed out that the average spectroscopic temperature even exceeds the median of the temperature distribution.

5.2.2. Entropy profile

As shown in Sect. 4.2, the most striking result of our analysis is that the combined X-SZ entropy profile is consistent at 1σ with the self-similar expectation once clumping-corrected gas density profiles are used. This implies that for Abell 2142, the formation history in the outskirts is similar to that expected from purely gravitational collapse (see, e.g., Voit et al. 2005). This shows that for this cluster spherical virialization shocks is the dominant source for building up the entropy level of the ICM. Since the accretion shocks are located at larger radii ($\sim 3 \times R_{200} \sim 6.5$ Mpc; Lau et al. 2015), we do not expect to observe a turnover in the entropy profile, even in the broad radial range accessible to this study. This conclusion is reinforced by the study performed in Cavaliere et al. (2011), where the authors found inverse correlations between the entropy level and the halo concentration, implying that for low halo concentration like A 2142, the entropy profile is expected to follow the self-similar expectations and to undergo negligible nonthermal support. A small contribution of clumps that are smaller than the resolution of our study (~20 kpc) could be invoked to bring the two measurements in agreement, although such a contribution is not required from a statistical point of view.

Conversely, when the effect of gas clumping is not taken into account, the entropy profile flattens beyond R_{500} and shows a behavior very similar to most of the studies based on *Suzaku* data (e.g., Urban et al. 2014; Akamatsu et al. 2011; Walker et al. 2013; Sato et al. 2014). In a study based on a sample of relaxed clusters, Walker et al. (2012) showed that all clusters exhibit a flattening in their entropy profile beyond R_{500}. The object A 2142 probably has the most significant turnaround in the entropy profile in their sample. Such a behavior has been interpreted in the past as evidence for a lack of thermalization in the gas at these radii because of the presence of a significant nonthermal pressure (e.g., Lapi et al. 2010; Kawaharada et al. 2010) or nonequilibration between ions and electrons (Hoshino et al. 2010; Avestruz et al. 2015). For instance, Fusco-Femiano & Lapi (2014) invoked the presence of a nonthermal pressure component to sustain hydrostatic equilibrium in the outskirts of A 1795, A 2029, A 2204, and A 133,

and concluded that the temperature profile steepening is mostly due to nonthermal effects, while the role of the gas clumping was assumed to be marginal (see also Walker et al. 2012). However, our results establish that clumping is the primary mechanism driving the entropy flattening and show that nonthermal effects, if present, should be mild. Interestingly, based on hydrodynamical simulations of galaxy cluster formation, Nelson et al. (2014) concluded that the nonthermal pressure accounts for only 10−30% of the total pressure support at R_{200}, while out-of-equilibrium electrons can cause a drop in temperature by 10% at R_{200} (Rudd & Nagai 2009; Avestruz et al. 2015). This implies that neither process seems sufficient to explain the observed entropy drop in the case where the clumping is not taken into account.

5.3. Hydrostatic mass and gas fraction

5.3.1. No hint of hydrostatic bias

As shown in Fig. 13 and Table 4, all the mass reconstructions presented here agree with the reconstructions based on weak gravitational lensing and galaxy dynamics (and even slightly exceed them). This is somewhat surprising, since the latter measurements do not require any assumptions about the state of the gas. Indeed, residual kinetic energy in the form of bulk motions or turbulence should induce an additional pressure term, which should lead to an underestimate of the mass when the energy budget is assumed to be entirely thermalized (e.g., Rasia et al. 2006; Nagai et al. 2007a; Burns et al. 2010). Simulations consistently predict that nonthermal effects should be proportionally larger beyond R_{500} (Lau et al. 2009; Battaglia et al. 2013). The lack of difference between hydrostatic-based and weak lensing measurements would therefore imply that the gas in the outskirts of A 2142 is relaxed and fully thermalized. This is a surprising result, especially since recent studies have unveiled that A 2142 is located at the core of a collapsing supercluster (Einasto et al. 2015; Gramann et al. 2015).

Although weak lensing is insensitive to the dynamical state, it is sensitive to the triaxiality of the observed halo (e.g., Limousin et al. 2013). Thanks to a large spectroscopic campaign totaling nearly 1000 redshifts, Owers et al. (2011) found that A 2142 does not show prominent substructures along the line of sight, but it is strongly elongated in the plane of the sky along the NW-SE axis. This could lead to an underestimation of the cluster mass when assuming spherical symmetry, both for weak lensing and galaxy kinematics, which might explain the slightly higher hydrostatic masses observed here all the way out to R_{200}.

We noted in Sect. 4.3 that the purely X-ray hydrostatic mass profile does not seem to be affected by the presence of clumps. This can be explained by the facts that (i) the hydrostatic mass depends on the logarithmic clumping factor gradient (see, e.g., Eq. (14) of Roncarelli et al. 2013), which is observed to be negligible (see Fig. 7); and (ii) the effect of the presence of clumps on the spectroscopic temperature is observed to be small as well (see Sect. 5.2.1). Therefore, the standard X-ray hydrostatic mass measurement technique is essentially unaffected. This is not the case of the X-SZ method, since in this case the gas density enters directly in the hydrostatic equation (Eq. (7)). This explains why the clumping-corrected X-SZ profile agrees with the X-ray-only result, while the mean X-SZ profile returns a mass that is lower by ∼20%.

5.3.2. Gas fraction

Depending on the adopted method, our measurements of the gas fraction (see Fig. 15) indicate a rather flat gas fraction, which is consistent with the universal value of the baryon fraction once the stellar fraction ($f_\star$) is taken into account, i.e., $\Omega_b/\Omega_m - f_\star \approx 13-14\%$. The gas fraction only slightly rises from the core to the outskirts, unlike what is usually observed in most clusters (e.g., Vikhlinin et al. 2006). Indeed, it is expected that the gas fraction should increase with the distance from the cluster center because of entropy injection (see, e.g., Pratt et al. 2010; Young et al. 2011).

As pointed out in Simionescu et al. (2011), Vazza et al. (2013), the effect of clumping is largest on the reconstructed gas fraction, since it combines a negative bias on the gravitating mass with a positive bias on the gas mass (see the discussion in Eckert et al. 2015). Comparing the gas fraction profiles obtained with and without the correction for the emissivity bias, we found that while the clumping-corrected gas fraction is roughly constant in the range 0.5−3 Mpc and consistent with the cosmic value corrected for the stellar fraction, the X-SZ gas fraction profile uncorrected for clumping increases with radius and exceeds the universal baryon fraction in the outskirts of the cluster. The classical X-ray analysis sits somewhat in between, since the hydrostatic mass measured with this method is relatively unaffected by clumping (see above), while the gas mass is overestimated.

A similar effect was observed in Eckert et al. (2013b), where the authors measured the average gas fraction in unrelaxed and relaxed clusters using the azimuthal mean density profile from ROSAT PSPC and the pressure profile from *Planck*. They observed that in non-cool-core clusters the gas fraction at R_{200} exceeds the universal value, while for the relaxed (cool-core) clusters the gas faction is consistent with the expectations. This difference could be explained by a larger amplitude in the inhomogeneities of the gas distribution in unrelaxed clusters than in relaxed clusters, which would lead to a larger clumping factor in the former class. Such a dependence is expected in numerical simulations, in which unrelaxed clusters are characterized by a larger mass accretion rate, and thus by a larger clumping factor. Our results show that in the case of A 2142 gas clumping alone can explain the observed excess gas fraction beyond R_{500}. This therefore reinforces this interpretation.

5.4. Reliability of the method in the presence of large substructures

Abell 2142 is a dynamically active cluster where an infalling galaxy group was discovered in the NE region (see caption of Fig. 1 and Eckert et al. 2014). With an estimated temperature of 1.3−1.5 keV, this accreted substructure is still not in thermodynamic equilibrium with the ICM of the main cluster. Therefore, the properties of the gas in NE region are not expected to be representative of the cluster ICM.

In order to quantify the effect of the presence of such a subcluster in our results, we repeated exactly the same procedure as above, but leaving out the NE region from our analysis. The results obtained excluding the NE region from the combined fits in the spectral analysis can be found in Tables D.2 and D.3. The results of the combined fit with and without the NE region are consistent, except for the value of the APEC norm in the 9−12 arcmin annulus, which increases when we remove the NE region from the analysis to the order of 1%. This effect could be due to statistical fluctuations.

We then applied the method of Ettori et al. (2010) to these profiles and obtained a hydrostatic mass profile that can be characterized by the quantities $M_{200} = 14.5 \pm 0.3 \times 10^{14}\ M_{\odot}$ and $R_{200} = 2270 \pm 17$ kpc. The comparison with the results obtained including the NE region (see Table 4) shows that masking the NE region changes the hydrostatic mass M_{200} by just 3%. This shows that our method can be applied even in the presence of substructures as long as their size does not exceed the size of this subcluster (whose mass has been estimated to be on the order of a few $10^{13}\ M_{\odot}$; see Eckert et al. 2014).

6. Conclusion

In this paper, we studied the outskirts of the massive cluster Abell 2142 by combining X-ray (*XMM-Newton*) and SZ (*Planck*) data, which allowed us to trace the state of the intracluster gas out to the virial radius of this system. For the first time, we applied a method that is insensitive to the presence of gas inhomogeneities with the aim of disentangling the effects of gas clumping and nonthermal pressure support. Our main findings can be summarized as follows:

- We found that Abell 2142 is affected by a significant level of clumping in its outskirts, which leads to a mean clumping factor $\sqrt{C} = 1.18 \pm 0.06$ at R_{200}. Roughly half of the clumping can be ascribed to the presence of large-scale asymmetries in the gas distribution, while the remaining half should be in the form of accreting clumps (see Fig. 16).
- We recovered the entropy profile of the cluster out to the virial radius by combining the gas density profile from *XMM-Newton* with the pressure profile from *Planck* (Fig. 12). We showed that when gas clumping is taken into account, the entropy profile follows the prediction of purely gravitational collapse (Voit et al. 2005). Indeed, the flattening of the entropy profile, which is significant when using the azimuthal mean density profile (see also Akamatsu et al. 2011), disappears when the X-ray analysis is corrected for the clumping bias. Therefore, contrary to Akamatsu et al. (2011) our data do not require us to invoke nongravitational effects to explain a lack of thermalization of the intracluster gas beyond R_{500}. We note however that the analysis performed in Akamatsu et al. (2011) was limited to the NW direction and that this lack of azimuthal coverage may contribute to their results.
- We applied the hydrostatic equilibrium equation to reconstruct the mass profile of the cluster out to its virial radius (Fig. 13). While the hydrostatic mass profile obtained with the azimuthal median is consistent with hydrostatic equilibrium assumption with the thermal gas, the hydrostatic mass profile obtained using the azimuthal mean decreases at R_{200} and beyond. This has been interpreted in several previous studies as evidence for a strong nonthermal pressure component to balance gravity. In Table 4, we compared our mass measurements to the results obtained with *Suzaku* (Akamatsu et al. 2011), to the weak lensing mass estimate from Umetsu et al. (2009), and to the galaxy kinematics measurement from Munari et al. (2014). Our mass estimates are consistent and even slightly exceed the estimates obtained with different methods, which does not require us to invoke a hydrostatic bias. Furthermore, the total mass estimated from the classical spectroscopic X-ray method is only slightly affected by gas clumping (this is a second order effect) and follows the X-SZ mass profile obtained with the azimuthal median. This may indicate that the temperature profile from spectroscopic analysis is mildly affected by the presence of clumps (Fig. 11).
- Finally, we combined our hydrostatic mass and gas mass measurements to estimate the radial profile of intracluster gas fraction (Fig. 15). Our results show that the profile obtained using a method insensitive to clumping is consistent with $\Omega_{\rm b}/\Omega_{\rm m} - f_{\star}$. Conversely, the gas fraction profile derived using the azimuthal mean increases in the cluster outskirts and exceeds the cosmic value.

In conclusion, the case of Abell 2142 provides a striking example of the importance of using a method that is insensitive to outliers in the gas distribution when probing the thermodynamical state of cluster outskirts. When correcting for gas clumping, the radial profiles of entropy, hydrostatic mass, and gas faction are consistent with the predictions. Conversely, when using the classical method (azimuthal mean), we observe a strong entropy flattening beyond R_{500} and a gas fraction that exceeds the cosmic values. Neglecting the clumping effect would therefore require us to invoke additional effects such as nonequilibration between ions and electrons (e.g., Akamatsu et al. 2011; Hoshino et al. 2010) or nonthermal pressure components to sustain gravity (e.g., Fusco-Femiano & Lapi 2014).

In the near future, the X-COP program will provide a similar data quality for a sizable cluster sample (13 clusters), which will allow us to test whether the conclusions drawn here in the case of A 2142 can be generalized to the local cluster population.

Acknowledgements. We thank F. Vazza for a careful reading of the manuscript. C.T. acknowledges the financial support from the Swiss National Science Foundation. E.P. and G.H. are grateful for the support of the French Agence Nationale de la Recherche under grant ANR-11-BS56-015. S.E., S.M., F.G. acknowledge the financial contribution from contracts ASI-INAF I/009/10/0 and PRIN-INAF 2012 "A unique dataset to address the most compelling open questions about X-Ray Galaxy Clusters". Based on observations obtained with *XMM-Newton*, as ESA science mission with instruments and contributions directly funded by ESA Member States and NASA.

References

Akamatsu, H., Hoshino, A., Ishisaki, Y., et al. 2011, PASJ, 63, 1019
Ameglio, S., Borgani, S., Pierpaoli, E., & Dolag, K. 2007, MNRAS, 382, 397
Ameglio, S., Borgani, S., Pierpaoli, E., et al. 2009, MNRAS, 394, 479
Anders, E., & Grevesse, N. 1989, Geochim. Cosmochim. Acta, 53, 197
Arnaud, M., Pratt, G. W., Piffaretti, R., et al. 2010, A&A, 517, A92
Avestruz, C., Nagai, D., Lau, E. T., & Nelson, K. 2015, ApJ, 808, 176
Basu, K., Zhang, Y.-Y., Sommer, M. W., et al. 2010, A&A, 519, A29
Battaglia, N., Bond, J. R., Pfrommer, C., & Sievers, J. L. 2013, ApJ, 777, 123
Battaglia, N., Bond, J. R., Pfrommer, C., & Sievers, J. L. 2015, ApJ, 806, 43
Bonamente, M., Landry, D., Maughan, B., et al. 2013, MNRAS, 428, 2812
Burns, J. O., Skillman, S. W., & O'Shea, B. W. 2010, ApJ, 721, 1105
Buote, D. A. 2000, ApJ, 539, 172
Carter, J. A., & Sembay, S. 2008, A&A, 489, 837
Carter, J. A., Sembay, S., & Read, A. M. 2011, A&A, 527, A115
Cavagnolo, K. W., Donahue, M., Voit, G. M., & Sun, M. 2009, ApJS, 182, 12
Cavaliere, A., Lapi, A., & Fusco-Femiano, R. 2011, ApJ, 742, 19
Croston, J. H., Arnaud, M., Pointecouteau, E., & Pratt, G. W. 2006, A&A, 459, 1007
De Luca, A., & Molendi, S. 2004, A&A, 419, 837
Eckert, D., Molendi, S., & Paltani, S. 2011, A&A, 526, A79
Eckert, D., Vazza, F., Ettori, S., et al. 2012, A&A, 541, A57
Eckert, D., Molendi, S., Vazza, F., Ettori, S., & Paltani, S. 2013a, A&A, 551, A22
Eckert, D., Ettori, S., Molendi, S., Vazza, F., & Paltani, S. 2013b, A&A, 551, A23
Eckert, D., Molendi, S., Owers, M., et al. 2014, A&A, 570, A119
Eckert, D., Roncarelli, M., Ettori, S., et al. 2015, MNRAS, 447, 2198
Eckert, D., Ettori, S., Coupon, J., et al. 2016, A&A, 592, A12
Einasto, M., Gramann, M., Saar, E., et al. 2015, A&A, 580, A69
Ettori, S., & Molendi, S. 2011, Mem. Soc. Astron. It. Suppl., 17, 47
Ettori, S., De Grandi, S., & Molendi, S. 2002, A&A, 391, 841

Ettori, S., Gastaldello, F., Leccardi, A., et al. 2010, A&A, 524, A68
Ettori, S., Donnarumma, A., Pointecouteau, E., et al. 2013, Space Sci. Rev., 177, 119
Fabian, A. C., Hu, E. M., Cowie, L. L., & Grindlay, J. 1981, ApJ, 248, 47
Farnsworth, D., Rudnick, L., Brown, S., & Brunetti, G. 2013, ApJ, 779, 189
Frank, K. A., Peterson, J. R., Andersson, K., Fabian, A. C., & Sanders, J. S. 2013, ApJ, 764, 46
Foreman-Mackey, D., Hogg, D. W., Lang, D., & Goodman, J. 2013, PASP, 125, 306
Fusco-Femiano, R., & Lapi, A. 2014, ApJ, 783, 76
Gonzalez, A. H., Zaritsky, D., & Zabludoff, A. I. 2007, ApJ, 666, 147
Górski, K. M., Hivon, E., Banday, A. J., et al. 2005, ApJ, 622, 759
Gramann, M., Einasto, M., Heinämäki, P., et al. 2015, A&A, 581, A135
Hoshino, A., Henry, J. P., Sato, K., et al. 2010, PASJ, 62, 371
Hurier, G., Macìas-Pérez, J. F., & Hildebrandt, S. 2013, A&A, 558, A118
Jarosik, N., Bennett, C. L., Dunkley, J., et al. 2011, ApJS, 192, 14
Kalberla, P. M. W., Burton, W. B., Hartmann, D., et al. 2005, A&A, 440, 775
Kawaharada, M., Okabe, N., Umetsu, K., et al. 2010, ApJ, 714, 423
Khedekar, S., Churazov, E., Kravtsov, A., et al. 2013, MNRAS, 431, 954
Kriss, G. A., Cioffi, D. F., & Canizares, C. R. 1983, ApJ, 272, 439
Kuntz, K. D., & Snowden, S. L. 2008, A&A, 478, 575
Lamarre, J.-M., Puget, J.-L., Ade, P. A. R., et al. 2010, A&A, 520, A9
Lapi, A., Fusco-Femiano, R., & Cavaliere, A. 2010, A&A, 516, A34
Lau, E. T., Kravtsov, A. V., & Nagai, D. 2009, ApJ, 705, 1129
Lau, E. T., Nagai, D., Avestruz, C., Nelson, K., & Vikhlinin, A. 2015, ApJ, 806, 68
Leccardi, A., & Molendi, S. 2008, A&A, 486, 359
Limousin, M., Morandi, A., Sereno, M., et al. 2013, Space Sci. Rev., 177, 155
Maccacaro, T., Gioia, I. M., Wolter, A., Zamorani, G., & Stocke, J. T. 1988, ApJ, 326, 680
Mathiesen, B., Evrard, A. E., & Mohr, J. J. 1999, ApJ, 520, L21
Markevitch, M., Ponman, T. J., Nulsen, P. E. J., et al. 2000, ApJ, 541, 542
Mazzotta, P., Rasia, E., Moscardini, L., & Tormen, G. 2004, MNRAS, 354, 10
McCammon, D., Almy, R., Apodaca, E., et al. 2002, ApJ, 576, 188
McLaughlin, D. E. 1999, AJ, 117, 2398
Mitsuda, K., Bautz, M., Inoue, H., et al. 2007, PASJ, 59, 1
Morandi, A., & Cui, W. 2014, MNRAS, 437, 1909
Morandi, A., Nagai, D., & Cui, W. 2013, MNRAS, 436, 1123
Moretti, A., Campana, S., Lazzati, D., & Tagliaferri, G. 2003, ApJ, 588, 696
Munari, E., Biviano, A., & Mamon, G. A. 2014, A&A, 566, A68
Nagai, D., & Lau, E. T. 2011, ApJ, 731, L10
Nagai, D., Kravtsov, A. V., & Vikhlinin, A. 2007a, ApJ, 668, 1
Nagai, D., Vikhlinin, A., & Kravtsov, A. V. 2007b, ApJ, 655, 98
Navarro, J. F., Frenk, C. S., & White, S. D. M., 1997, ApJ, 490, 493
Nelson, K., Lau, E. T., & Nagai, D. 2014, ApJ, 792, 25
Nevalainen, J., David, L., & Guainazzi, M. 2010, A&A, 523, A22
Nord, M., Basu, K., Pacaud, F., et al. 2009, A&A, 506, 623
Okabe, N., Umetsu, K., Tamura, T., et al. 2014, PASJ, 66, 99
Owers, M. S., Nulsen, P. E. J., Couch, W. J., & Markevitch, M. 2009, ApJ, 704, 1349
Owers, M. S., Nulsen, P. E. J., & Couch, W. J. 2011, ApJ, 741, 122
Piffaretti, R., Arnaud, M., Pratt, G. W., Pointecouteau, E., & Melin, J.-B. 2011, A&A, 534, A109
Planck Collaboration Int. I. 2012, A&A, 543, A102
Planck Collaboration Int. V. 2013, A&A, 550, A131
Planck Collaboration XXI. 2014, A&A, 571, A21
Planck Collaboration XXXII. 2015, A&A, 581, A14
Planck Collaboration I. 2016, A&A, 594, A1
Planck Collaboration XIII. 2016, A&A, 594, A13
Planck Collaboration XXII. 2016, A&A, 594, A22
Planck Collaboration XXVII. 2016, A&A, 594, A27
Planck HFI Core Team 2011, A&A, 536, A4
Pratt, G. W., Arnaud, M., Piffaretti, R., et al. 2010, A&A, 511, A85
Rasia, E., Ettori, S., Moscardini, L., et al. 2006, MNRAS, 369, 2013
Rasia, E., Lau, E. T., Borgani, S., et al. 2014, ApJ, 791, 96
Reiprich, T. H., Hudson, D. S., Zhang, Y.-Y., et al. 2009, A&A, 501, 899
Reiprich, T. H., Basu, K., Ettori, S., et al. 2013, Space Sci. Rev., 177, 195
Roncarelli, M., Ettori, S., Borgani, S., et al. 2013, MNRAS, 432, 3030
Rossetti, M., Eckert, D., De Grandi, S., et al. 2013, A&A, 556, A44
Rozo, E., Vikhlinin, A., & More, S. 2012, ApJ, 760, 67
Rudd, D. H., & Nagai, D. 2009, ApJ, 701, L16
Sato, K., Matsushita, K., Yamasaki, N. Y., Sasaki, S., & Ohashi, T. 2014, PASJ, 66, 85
Sayers, J., Czakon, N. G., Mantz, A., et al. 2013, ApJ, 768, 177
Simionescu, A., Allen, S. W., Mantz, A., et al. 2011, Science, 331, 1576
Snowden, S. L., McCammon, D., Burrows, D. N., & Mendenhall, J. A. 1994, ApJ, 424, 714
Snowden, S. L., Mushotzky, R. F., Kuntz, K. D., & Davis, D. S. 2008, A&A, 478, 615
Smith, R. K., Brickhouse, N. S., Liedahl, D. A., & Raymond, J. C. 2001, ApJ, 556, L91
Sunyaev, R. A., & Zeldovich, Y. B. 1972, Comm. Astrophys. Space Phys., 4, 173
Tauber, J. A., Mandolesi, N., Puget, J.-L., et al. 2010, A&A, 520, A1
Umetsu, K., Birkinshaw, M., Liu, G.-C., et al. 2009, ApJ, 694, 1643
Urban, O., Simionescu, A., Werner, N., et al. 2014, MNRAS, 437, 3939
Vazza, F., Brunetti, G., Kritsuk, A., et al. 2009, A&A, 504, 33
Vazza, F., Roncarelli, M., Ettori, S., & Dolag, K. 2011, MNRAS, 413, 2305
Vazza, F., Eckert, D., Simionescu, A., Brüggen, M., & Ettori, S. 2013, MNRAS, 429, 799
Vikhlinin, A., Kravtsov, A., Forman, W., et al. 2006, ApJ, 640, 691
Voges, W., Aschenbach, B., Boller, T., et al. 1999, A&A, 349, 389
Voit, G. M., Kay, S. T., & Bryan, G. L. 2005, MNRAS, 364, 909
Walker, S. A., Fabian, A. C., Sanders, J. S., & George, M. R. 2012, MNRAS, 427, L45
Walker, S. A., Fabian, A. C., Sanders, J. S., Simionescu, A., & Tawara, Y. 2013, MNRAS, 432, 554
Young, O. E., Thomas, P. A., Short, C. J., & Pearce, F. 2011, MNRAS, 413, 691
Zhuravleva, I., Churazov, E., Kravtsov, A., et al. 2013, MNRAS, 428, 3274

Appendix A: Modeling residual soft protons

In the considered soft band, soft protons provide a modest but non-negligible contribution, and to account for this contribution we need to follow a complex procedure. We start by deriving a spectral model for the quiescent particle background (QPB), over a broad spectral range, by making use of spectra extracted over the full FOV from the auxiliary background event files. The model comprises a broken power law with different parameters for MOS and pn, and several Gaussian lines to account for fluorescent emission that is observed in both detectors. We excise spectral regions that are polluted by particularly intense lines, as they are not particulary helpful in constraining the shape of the continuum. We then fit the spectra extracted over the full FOV from the event files of the observation with a model comprising a QPB component plus a quiescent soft proton background (QSP) component. For the QPB component, the parameters are fixed to those derived from the fit of the auxiliary background data. For the QSP component, which has the form of a broken power law, all parameters, with the exception of the normalization, are fixed to fiducial values (see Kuntz & Snowden 2008; Leccardi & Molendi 2008, for a detailed analysis). The fit is carried out in the hard X-ray band where the QSP contribution is more significant and therefore more easily gauged. More specifically, for the MOS we use the [4.0−11.5] keV band while for the pn the [4.0−7.1] keV and [9.2−14.0] keV bands the region between 7.1 and 9.2 keV is excluded to avoid the strong fluorescence lines that are found there. We verified that adopting a somewhat more restrictive range, i.e., excluding the [4.0−5.0] keV band, has a negligible effect on the derived parameters and on the test presented in Appendix B. Finally the parameters of the soft proton component are fed to the ESAS task `proton`, which produces a soft proton image in the 0.7−1.2 keV band for each of the three detectors. In Fig. A.1 we provide an example of a fit to the MOS2 Spectrum for observation 0085150101.

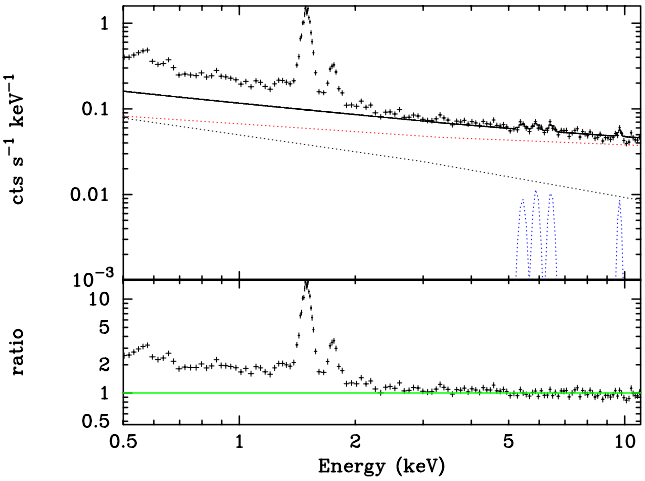

Fig. A.1. MOS2 Spectrum for observation 0085150101 (see Table A.1) accumulated over the entire FOV. *Top panel*: observed spectrum (data points) and spectral model comprising a QPB component (broken power law, shown as a dashed red line, and Gaussian lines, shown as dashed blue lines) and a QSP component (broken power law, shown as a dashed black line). The fit is performed in the [4−10] keV energy range and extrapolated to lower energies. Parameters for the QPB component are fixed to the value estimated from filter-wheel-closed data. The contribution of the QSP component increases with respect to that of the QPB as we move down in energy. *Bottom panel*: residuals in the form of ratio of data over model; in the [0.7−1.2] keV band the data exceeds the model by a factor of 2, indicating that in this range roughly half of the accumulated events come from the X-ray sky and the other half are associated with particles.

Appendix B: Assessment of systematic uncertainties

Given the different radial dependence of the various background components, i.e., cosmic background, QPB, and QSP, an indication of the quality of our methodology can be obtained by producing a mean cosmic background radial profile by stacking a large number of blank-field observations. The stacking process allows us to: (1) average out any significant gradient in the radial directions associated either with cosmic variance or structure in the Galactic foreground; and (2) achieve sufficient statistics to address systematic issues at the few percent level. We chose 21 observations from the *XMM-Newton* archive; a subsample of these were previously analyzed and discussed elsewhere (Leccardi & Molendi 2008). The sample covers most of the mission timeline, and the bulk of the observations have equivalent hydrogen column densities $N_{\rm H} < 3 \times 10^{20}$ cm^{-2}, while a few are between 3×10^{20} cm^{-2} and a few 10^{21} cm^{-2}. The total observing time after flare removal is roughly 1.3 Ms for MOS1 and MOS2 and 1 Ms for pn. Details on the sample can be found in Table A.1. For each observation, we use the ESAS task `comb` to produce a MOS1 + MOS2 + pn counts image of the field and an associated exposure map. The latter is obtained by summing the exposure maps for the three different detectors using appropriate weights for each detector. The `comb` task is also used to produce a combined background image for the three detectors. The combined field image, background image, and exposure map are then fed into a program that produces a radial profile by taking the combined image counts in a given annulus, subtracting the counts from the same region of the background image, and dividing the resulting net counts by the mean exposure in the annulus and the area of the annulus.

Poisson errors from the counts in the field and background image annuli are propagated to derive statistical errors on the profile. Finally a mean radial profile is derived for the 21 observations by performing an error weighted mean for each annulus. In the bottom panel of Fig. B.1 we show a normalized version of this profile. As we can see, with the exception of the innermost arcminute, the radial profile is flat to within 10% everywhere with many data points within the 5% limit. An important point is that there is no evidence of a large scale trend, i.e., deviations around the mean are scattered over the full radial range and not clustered in a specific region. Regarding the central arcminute, there are a number of possible explanations for the observed drop in surface brightness. This observed drop could be related to poorly removed central sources, insufficiently accurate estimation of the aim point, loss of quantum efficiency in the region of the detectors subject to most intense X-ray irradiation, or to a combination of these explanations. Most importantly, however, this region is very small at less than 1% of the FOV and, therefore, it is not particularly important for our surface brightness estimates.

A fit to the surface-brightness profile with a constant, excluding the central arcminute, yields a χ^2 of 34.9 for 25 d.o.f. and an associated probability of 9% for the profile to be consistent with being flat, confirming that systematic deviations must be at the few percent level or smaller. To quantify the presence of residual systematics in our radial profile, we performed an analysis of the scatter. We modeled the intrinsic scatter in the

Table A.1. Blank field observations used to validate the surface-brightness production procedure.

Obs. Id.	Obs. Date [yr/mm/dd]	N_H [10^{20} cm^{-2}]	t_{M1} [ks]	t_{M2} [ks]	t_{pn} [ks]	$\mathcal{R}_{M1}$	$\mathcal{R}_{M2}$	$\mathcal{R}_{pn}$
0085150101	2001-10-15	2.8	37.6 38.6	31.3	1.15	1.19	1.11	
0094310201	2002-12-15	4.4	60.8	61.4	53.1	1.07	1.10	1.07
0108060701	2002-01-14	0.7	70.7	71.1	58.2	1.22	1.27	1.18
0108062301	2002-01-23	0.7	71.7	72.5	57.4	1.05	1.12	1.07
0109661001	2001-06-23	0.8	60.5	60.3	47.1	1.09	1.12	1.03
0111550401	2001-06-01	1.0	79.5	80.6	65.0	1.08	1.16	1.05
0112370101	2000-07-31	2.0	34.1	36.7	23.5	1.12	1.18	1.07
0112370301	2000-08-04	2.0	33.6	34.3	26.2	1.15	1.19	1.11
0128531601	2003-12-12	1.8	68.6	69.3	56.2	1.08	1.17	1.09
0147511701	2002-12-04	0.6	88.6	88.9	73.6	1.08	1.09	1.06
0147511801	2002-12-06	0.6	69.2	71.8	46.0	1.11	1.14	1.06
0148560501	2003-05-22	2.6	56.3	57.7	0.0	1.10	1.13	1.00
0148960101	2003-05-12	3.1	38.1	39.6	32.2	1.12	1.12	1.02
0203362101	2004-12-09	1.8	59.4	59.3	51.0	1.06	1.07	1.07
0210280101	2005-04-09	2.5	70.1	69.5	58.1	1.07	1.10	1.04
0302420101	2005-07-08	3.9	72.2	72.9	53.9	1.21	1.23	1.15
0303260201	2005-04-07	0.6	43.5	43.6	35.5	1.08	1.09	1.03
0402530201	2006-06-04	29.3	82.5	84.1	65.0	1.04	1.06	1.00
0500500701	2007-05-19	6.1	49.4	68.2	35.7	1.08	1.07	1.04
0555780101	2008-07-05	0.7	81.2	87.5	50.1	1.07	1.09	1.01
0651900201	2010-06-11	1.4	77.2	86.1	49.9	1.09	1.10	0.87

Notes. Column description: 1) observation identifier; 2) observation date; 3) equivalent hydrogen column density as estimated from 21 cm maps (Kalberla et al. 2005); 4) exposure time for MOS1 detector after flare removal; 5) exposure time for MOS2 detector after flare removal; 6) exposure time for pn detector after flare removal; 7) ratio of counts from observation over counts for auxiliary background event files for MOS1 detector. The ratio is computed over the full FOV and in the [7.5−11.85] keV energy band; 8) ratio of counts from observation over counts for auxiliary background event files for the MOS2 detector. The ratio is computed over the full FOV and in the [7.5−11.85] keV energy band; 9) ratio of counts from observation over counts for auxiliary background event files for the pn detector. The ratio is computed over the full FOV and in the [9.2−14.0] keV energy band.

form of a Gaussian. We used a maximum likelihood algorithm (Maccacaro et al. 1988) to fit the mean radial profile and its errors, where the free parameters are the mean and intrinsic scatter (i.e., the standard deviation of the Gaussian). Our algorithm returns a mean for the profile of 0.99 ± 0.01, which is not surprising, as the profile is normalized. More interestingly, the intrinsic scatter is 0.04 ± 0.01, implying that systematic deviations from flatness are less than 5%.

Profiles for the individual detectors, i.e., MOS1, MOS2, and pn, are consistent with the profile averaged over all instruments. We also tried cutting our sample in different ways: low and high N_H, low and high residual soft proton component, and the early and late part of the mission. In no instance do we detect a substantial deviation from the mean profile. For comparison, in the top panel of Fig. B.1 we also plot a radial profile that was produced without taking the residual soft proton component into account, i.e., only the QPB image was subtracted from the observation image. At variance with the black profile, the red profile shows deviations that go up to 15%. The most important difference is that this profile is not flat but rises steadily so that at edge of the FOV it is about 30% higher than at the center (excluding the central arcminute), which clearly shows that the failure to remove the residual soft proton contribution results

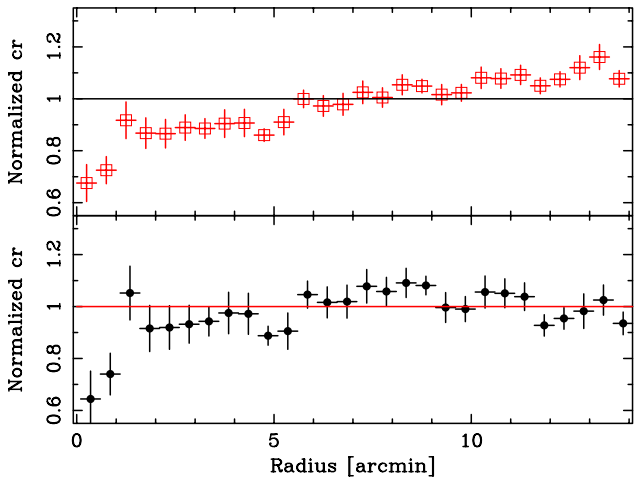

Fig. B.1. Stacked normalized EPIC surface-brightness profile for 21 blank fields (see Table A.1). *Top panel*: profile produced without accounting for the QSP component. The surface brightness increases steadily moving from the center to outer regions of the detectors. *Bottom panel*: profile produced after subtraction of the QSP component. Beyond the innermost arcminute, the profile is flat, within deviations contained within 5%−10%.

in a significant systematic error on extended sources with surface brightness comparable to that of the X-ray background. In conclusion, the method presented here is able to estimate the total background with a precision of 5% in the [0.7−1.2] keV band. This allows us to extract the surface-brightness profiles of A 2142 out to $\sim 2 \times R_{500}$, where systematic and statistical uncertainties become comparable.

Appendix C: Comparison between *XMM-Newton* and ROSAT results

As a final validation of the background subtraction method presented in this paper, we compared the background-subtracted surface-brightness profile of A 2142 with the surface-brightness profile of the same system measured with ROSAT PSPC. Thanks to its very wide FOV (∼2 square degrees) and very low instrumental background, ROSAT PSPC was very well suited to measure low surface-brightness emission. The ROSAT data were reduced using the ESAS data reduction scheme (Snowden et al. 1994) following the method described in Eckert et al. (2012). The profiles were converted into energy flux by assuming that the spectral shape is reproduced by an absorbed APEC model at a temperature of 8 keV, and folding the spectral model with the response of the two instruments. The resulting profiles are shown in Fig. C.1. A remarkable agreement is observed out to the largest radii probed, which correspond to $1.3 \times R_{200} \sim 3000$ kpc.

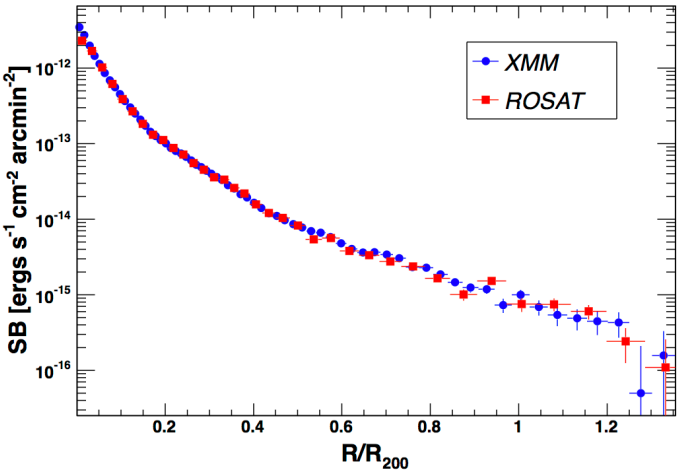

Fig. C.1. Surface-brightness profiles of A 2142 obtained with *XMM-Newton* (blue) and ROSAT PSPC (red) converted into energy flux in the [0.5−2] keV band. In the x axis we show the distance to the cluster center divided by $R_{200} \sim 2200$ kpc.

Appendix D: Tables and spectra

D.1. Spectra of each of the annuli defined in Fig. 1

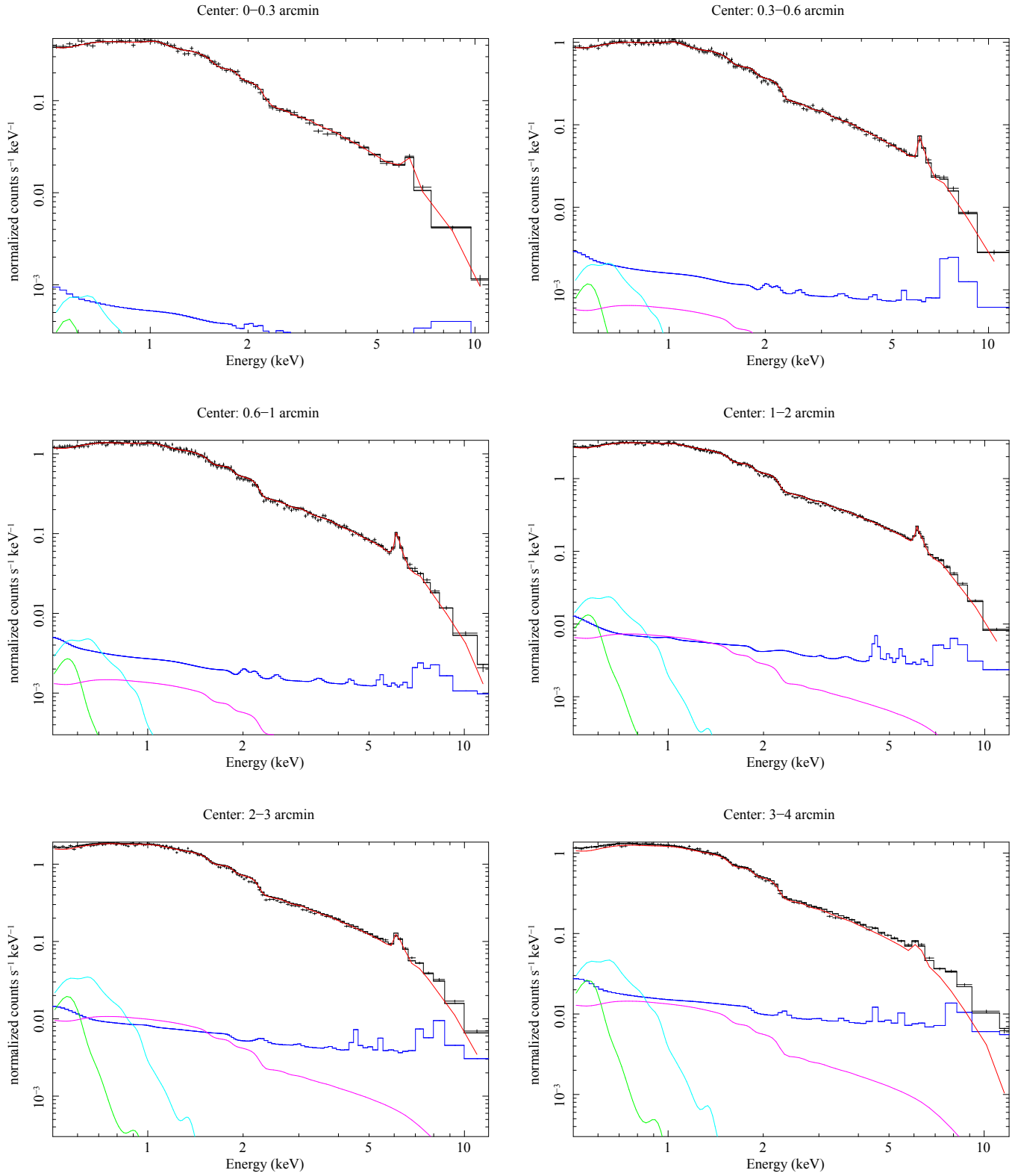

Fig. D.1. EPIC pn spectra for the annuli defined in Fig. 1. The various components used for the fit are shown in red for the source; in blue for the NXB; in magenta for the CXB; in cyan for the Galactic halo emission; and in green for the local hot bubble. The fit was performed jointly on all 3 EPIC instruments, but here only the pn is shown for clarity. The results of the fit are listed in Table 3.

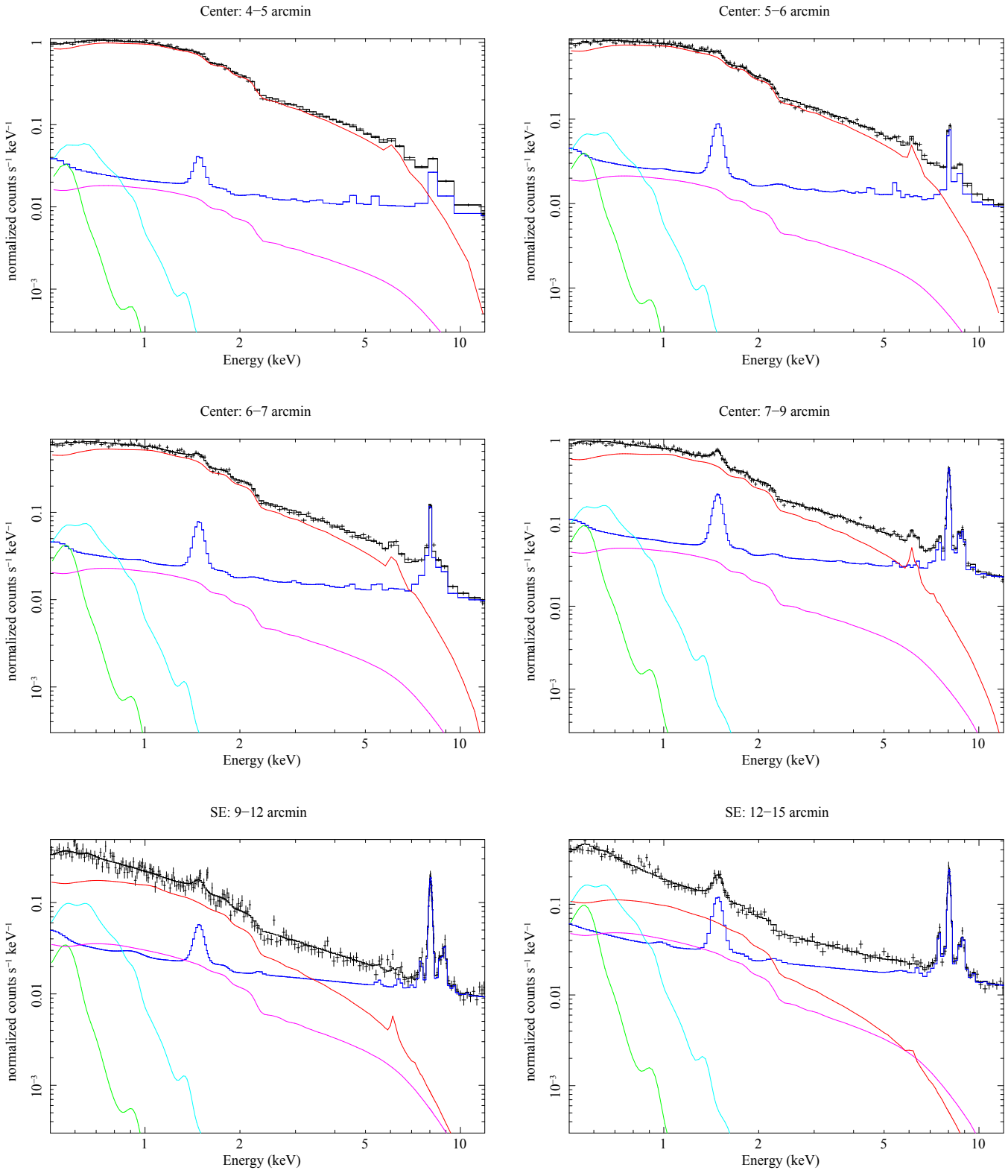

Fig. D.1. continued.

D.2. Results of the fit of the region in each observation individually

Table D.1. Result of the fit of the spectrum in the annulus 7−9 arcmin for the individual regions: center, NW, SE, and SW separately.

Obs.	T	ΔT	Norm	Δnorm	Z	ΔZ
Center	7.82	[7.66, 8.06]	0.0574	[0.0569, 0.0579]	0.346	[0.314, 0.387]
NW	7.28	[6.59, 8.15]	0.0441	[0.0424, 0.0456]	0.488	[0.319, 0.686]
SE	5.69	[5.40, 5.98]	0.104	[0.102, 0.105]	0.169	[0.116, 0.228]
SW	6.47	[5.69, 7.11]	0.0347	[0.0334, 0.0365]	0.249	[0.108, 0.423]

Notes. The results of the fit of the combined center, NW, SE, and SW regions can be found in Table 3. The temperature is given in keV, the norm in 10^{-3} cm^{-5}, and the abundance in solar metallicity.

Table D.2. Result of the fit of the spectrum in the annulus 9−12 arcmin for the individual regions: center, NE, NW, SE, and SW separately and for the combined fit excluding the NE region ($\mathrm{ALL_{withoutNE}}$).

Obs.	T	ΔT	Norm	Δnorm	Z	ΔZ
Center	7.25	[6.87, 7.63]	0.0241	[0.0238, 0.0245]	0.197	[0.143, 0.255]
NE	5.15	[4.50, 6.27]	0.0155	[0.0147, 0.0162]	0.0590	[0.0, 0.220]
NW	7.22	[6.62, 7.82]	0.0213	[0.0208, 0.0221]	0.152	[0.0, 0.342]
SE	5.28	[4.95, 5.76]	0.0240	[0.0235, 0.0243]	0.122	[0.0518, 0.200]
SW	4.75	[4.20, 5.32]	0.0153	[0.0147, 0.0159]	0.0949	[0.0, 0.219]
$\mathrm{ALL_{withoutNE}}$	7.17	[6.81, 7.44]	0.0229	[0.0226, 0.0231]	0.196	[0.153, 0.242]

Notes. The results of the combined fit including the NE region (center, NE, NW, SE, and SW) can be found in Table 3. The temperature is given in keV, the norm in 10^{-3} cm^{-5}, and the abundance in solar metallicity.

Table D.3. Result of the fit of the spectrum in the annulus 12−15 arcmin for the individual regions: NE, NW, SE, and SW separately and for the combined fit excluding the NE region ($\mathrm{ALL_{withoutNE}}$).

Obs.	T	ΔT	Norm	Δnorm	Z	ΔZ
NE	2.95	[2.60, 3.32]	0.00747	[0.00696, 0.00788]	0.333	[0.230, 0.477]
NW	6.87	[6.01, 8.82]	0.00858	[0.00801, 0.00921]	0.440	[0.139, 0.858]
SE	5.89	[5.18, 6.68]	0.00951	[0.00916, 0.00985]	0.117	[0.00914, 0.266]
SW	3.16	[2.75, 3.80]	0.00750	[0.00706, 0.00792]	0.0272	[0.0, 0.137]
$\mathrm{ALL_{withoutNE}}$	5.20	[4.75, 5.76]	0.00849	[0.00824, 0.00875]	0.140	[0.0530, 0.237]

Notes. The results of the combined fit including the NE region (NE, NW, SE, and SW) can be found in Table 3. The temperature is given in keV, the norm in 10^{-3} cm^{-5} and the abundance in solar metallicity.

D.3. XMM temperature profile in the NW direction

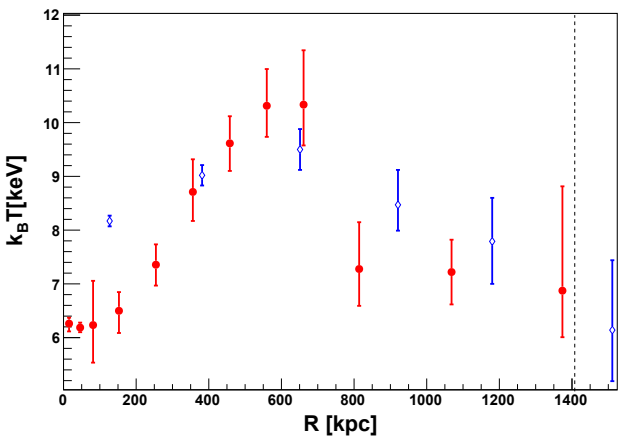

Fig. D.2. Temperature profile in the NW direction. Red: data points using the APEC model on *XMM-Newton* observations. In blue: data point from Akamatsu et al. (2011) obtained with *Suzaku*. The dashed line represents the value of R_{500}.